THE DYNAMIC RESPONSE OF STEEL BEAM-COLUMN ELEMENTS UNDER BLAST LOADING

A THESIS SUBMITTED TO
THE GRADUATE SCHOOL OF NATURAL AND APPLIED SCIENCES
OF
MIDDLE EAST TECHNICAL UNIVERSITY

BY

MEBRURE ITIR GEVREK

IN PARTIAL FULFILLMENT OF THE REQUIREMENTS
FOR
THE DEGREE OF MASTER OF SCIENCE
IN
CIVIL ENGINEERING

APRIL 2016

Approval of the thesis:

THE DYNAMIC RESPONSE OF STEEL BEAM-COLUMN ELEMENTS UNDER BLAST LOADING

submitted by **MEBRURE ITIR GEVREK** in partial fulfillment of the requirements for the degree of **Master of Science in Civil Engineering Department, Middle East Technical University** by,

Prof. Dr. M. Gülbin Dural Ünver _____
Dean, Graduate School of **Natural and Applied Sciences**

Prof. Dr. İsmail Özgür Yaman _____
Head of Department, **Civil Engineering**

Prof. Dr. Çetin Yılmaz _____
Supervisor, **Civil Engineering Dept., METU**

Examining Committee Members:

Assoc. Prof. Dr. Özgür Kurç _____
Civil Engineering Dept., METU

Prof. Dr. Çetin Yılmaz _____
Civil Engineering Dept., METU

Assoc. Prof. Dr. Yalın Arıcı _____
Civil Engineering Dept., METU

Assoc. Prof. Dr. Alp Caner _____
Civil Engineering Dept., METU

Assoc. Prof. Dr. Tolga Akış _____
Civil Engineering Dept., Atılım Üniversitesi

Date: **26.04.2016**

I hereby declare that all information in this document has been obtained and presented in accordance with academic rules and ethical conduct. I also declare that, as required by these rules and conduct, I have fully cited and referenced all material and results that are not original to this work.

Name, Surname: Mebrure Itır GEVREK

Signature:

ABSTRACT

THE DYNAMIC RESPONSE OF STEEL BEAM-COLUMN ELEMENTS UNDER BLAST LOADING

Gevrek, Mebrure Itır

M.S., Department of Civil Engineering

Supervisor: Prof. Dr. Çetin Yılmaz

April 2016, 93 pages

The intensity of terrorist activities and threats have become a major problem in modern world. Several factors in the way modern societies live have made easier to conduct terrorism activities. Developed societies are dependent on complex and vulnerable systems that could be target, such as railways, pipelines, large shopping areas, airlines, subway systems and large business/trade centers. The increase in the number of domestic and international terrorist activities by each passing day have forced researchers to examine the behavior of structures to blast loads. In order to get a better understanding of how structural elements behave under blast loading, a number of analytical methods were developed to predict the response of steel members subjected to blast loading. The prediction of element behavior during blast loading is a complex problem given the effect of geometry and the material nonlinearity on the response. Therefore, it is needed to verify the results of analytical methods used to predict the behavior of structural elements under blast loading and to understand the effect of the model parameters on the prediction results. In this study, first, experimental results were used to verify the analytical methods. General purpose finite element software ABAQUS was used to analyze steel beam-columns subjected to blast loading and the material model parameters were calibrated. Two

models, one in elastic range, the other undergoing plastic deformation were used in the calibration study. Sensitivity analyses were then conducted to understand the effect of the many modeling and loading parameters, including material models, boundary conditions and loading assumptions, on the predicted results for the blast loading of columns.

Keywords: Blast, three dimensional dynamic analysis, ABAQUS, Johnson-Cook constitutive model

ÖZ

ÇELİK KİRİŞ-KOLON ELEMANLARIN PATLAMA YÜKÜ ALTINDA DİNAMİK DAVRANIŞLARININ İRDELENMESİ

Gevrek, Mebrure Itır

Yüksek lisans, İnşaat Mühendisliği Bölümü
Tez Yöneticisi: Prof. Dr. Çetin Yılmaz

Nisan 2016, 93 sayfa

Günümüz dünyasında, terörist saldırı ve tehditlerin yoğunluğu büyük bir problem haline gelmiştir. Modern toplumların yaşam tarzındaki birçok faktör terörist aktivitelerin gerçekleştirilmesinde kolaylaştırıcı rol oynamaktadır. Gelişmiş toplumlar saldırılar için hedef olabilecek demiryolu, boru hatları, büyük alışveriş merkezleri, havayolları, metro sistemleri, büyük ticaret merkezleri gibi karmaşık ve hassas sistemlere muhtaçtır. Ulusal ve uluslararası alanda her geçen gün artan saldırılar araştırmacıları yapıların patlama yükü altında davranışını incelemeye yönlendirmiştir. Yapı elemanlarının patlama yükü altında nasıl davrandığının daha iyi anlaşılabilmesi için patlama yüküne maruz kalan çelik elemanların davranışını tahmin etmekte kullanılan birçok analitik metod geliştirilmiştir. Patlama yüküne mağruz kalan çelik elemanların davranışını tahmin etmek malzeme özellikleri ve geometrideki lineer olmama durumundan ötürü karmaşık bir problemdir. Bu yüzden patlama yüküne maruz kalan yapı elemanlarının davranışını tahmin etmekte kullanılan analitik metod sonuçlarının doğruluğunu ispat etmek ve model parametrelerinin tahmin sonuçlarındaki etkilerini anlamak gereklidir. Bu çalışmada analitik metotların doğruluğunu ispatlamak için deney sonuçları kullanılmıştır. Patlama yüküne maruz kalan çelik kiriş-kolon elemanların analizi genel kullanım

amaçlı sonlu eleman programı ABAQUS ile yapılmış ve malzeme modeli parametreleri kalibre edilmiştir. Kalibrasyon çalışmasında biri elastik bölgede kalan diğeri ise plastik deformasyon gösteren iki model kullanılmıştır. Malzeme modeli, sınır koşulları ve yükleme varsayımlarını içeren bir çok malzeme ve yükleme parametresinin etkisini anlamak için patlama yükü altındaki kolonların tahmin edilmiş sonuçları üzerinde hassasiyet analizleri yapılmıştır.

Anahtar Kelimeler: patlama, üç boyutlu dinamik analiz, ABAQUS, Johnson- Cook konstitütif model

To My Beloved Family and Husband…

ACKNOWLEDGEMENTS

I would like to thank to my advisor Prof. Dr. Çetin Yılmaz. I would also like to thank to Assoc. Prof. Dr. Özgür Kurç for his guidance and Assoc. Prof. Dr. Yalın Arıcı for his invaluable efforts.

I deeply thank to my sister Burcu and my brother Muharrem Altuğ for believing in me throughout my life. I would also thank to my parents Hülya and Ahmet for their constant encouragement and most importantly for endless love through all my life.

I would like to present my thanks to Halil Fırat Özel and Mehran Ghasabeh for their endless support and priceless helps that served me a lot.

I would also like express my thanks to my friends Buse Kurt and Can Kurt for their friendship and encouragement. I feel lucky to have their invaluable friendship.

I would like to acknowledge the invaluable moral support provided by Dr. Demet Cavcav. I am very thankful for her endless understanding.

Last, but not least, I would like to express my heartfelt thanks to my husband İsmail. Without his limitless encouragement and his everlasting patience this thesis would not have been possible. I have learned a lot of from his attitude to life and I am grateful for having his love. I dedicate this study to him.

Finally, I would like to thank to D. Bowie and F. Mercury for his song "Under Pressure" that provide me motivation throughout my study.

TABLE OF CONTENTS

LIST OF TABLES

TABLES

LIST OF FIGURES

FIGURES

CHAPTER 1

INTRODUCTION

1.1 Introduction

Terrorist organizations around the world have been using vehicle bombs for decades as an effective means to attack city centers. The effect of an explosion within or adjacent to a building can cause catastrophic damage to both the facade and internal structural frame, collapsing walls, blowing out windows and shutting down critical safety systems. Direct blast effects, structural collapse, fire and smoke can all result in injury and death to occupants and anyone who happens to be near the explosion. Additional casualties are often contributed to by indirect effects which can combine to inhibit or prevent timely evacuation of the structure.

Considering the effects of blast loads in structural design became a necessity with the increasing number of terrorist attacks. In order to develop a full understanding about the blast effect and take into account at the design stage, it is necessary to investigate this phenomenon. Many researchers suggested empirical formulas to estimate the characteristics of the blast wave in the past five decades. Although the data obtained from experimental studies had been used to set empirical formulas, experimental data are scarce in unclassified literature.

1.2 Literature Review

Often large dynamic loads, much greater than the original design loads of many structures, can cause major catastrophes resulting from gas or chemical explosions. Efforts have been made in the last few decades to develop new methods of structural analysis and design that resist blast loads due to the threat from such extreme load conditions. A detailed understanding of the chemistry and physics behind a blast and

the dynamic response of various structural elements is required for the analysis and design of structures subjected to blast loads. However, it should be mentioned that most of the studies in this area are carried out by defense agencies and therefore classified, leading to a limited field of literature on the subject.

Blast load software, such as CONWEP (Hyde, 1990) and ATBLAST (2007) are often used to determine the magnitude of loading on structural members. The loading profile obtained from these software is often used in general purpose finite element programs such as ABAQUS (2010) and LS-DYNA (2013) to simulate blast loads effects on structures. In such an analysis, the effect of blast loading on buried shelters, caused by conventional weapon detonation, was investigated Yang (1997) considering the effects of the soil damping, the stiffness and dimensions of the structure and the stand-off distance by using ABAQUS. Yang (1997) stated that because of the ground surface reflection of the blast wave, slight asymmetric deformation occurs on the wall of shelter. A comprehensive overview of the effects of the explosion on structures was done by Ngo et. al. (2007) comparing different methods to estimate the blast loads and structural response concluding the necessity to update the current Building Regulations and Design Standards by adding a guidelines on abnormal load cases and provisions on progressive collapse prevention. The effect of fire on blast loaded systems was considered by Liew (2007), showing the initial deformation in the form of permanent deflection caused by blast loads decreased the load carrying capacity of the columns in fire. The effect of blast loading on W-shaped steel columns was investigated by Lee et al. (2009) showing that the CFD software showed a definite rise time for loading, while the rise time obtained from blast software CONWEP and ATBLAST was negligible. The pressure peak and the time durations were almost same in each of the software. There were also some variations in the impulse distribution that was reflected through the columns. The analysts described the variations in the impulse division and the time profile of pressure was due to the irregularities in the rigidity of the surfaces of the different models. Although simulating the blast load based on computational fluid dynamics (CFD) can be very computationally intensive, complex structural geometry and oblique surfaces require such an approach. A new method to use finite element

approach with a Lagrangian structure and Eulerian meshed body of air was proposed by Mougette et al. (2010) using ABAQUS explicit. The results of the study look promising and the complex geometries could be analyzed by using this approach. The nonlinear behavior of SDOF systems under blast loading was investigated by Assal (2010) with two different types of blast loading. The displacement time history diagrams of simple pulse function and bilinear pulse function were compared and resulted displacement of bilinear pulse function was lesser than the other one. Cabello (2011) used ABAQUS explicit finite element software to analyze the effect of blast loading on Stainless Steel Plate. The blast wave profile was obtained from ConWEP (Conventional Weapons Effects) and material model represented by Johnson-Cook Constitutive Model. The different blast load conditions were investigated by changing the weight of charge. The steel plate subjected to explosion caused by detonation of 0.50 kg TNT equivalent explosive with the stand-off distance as 0.20 m deformed elastically. As the weight of charge increased to 1 kg TNT, the steel plate had undergone plastic deformation. The effect of loading on structure as a whole after the blast event was investigated by Guzas et al. (2011) using bounding surface plasticity models for steel wide flange elements. Avoiding high resolution modeling tools, the approach presents the system as a whole with a database of bounding surfaces for various wide-flange members. The study showed that computationally efficient evaluation of effect of the blast load could be achieved by using bounding surface plasticity model database. The efficiency of the façade systems that had been designed to resist lateral blast loading was studied by using conventional structural analysis tools by McKay et al. (2011) as a part of the "Steel Frame Structure Performance in Blast Environments" research program (USDOD). One of the most important inferences of this study was the bracing system showing increased resistance to blast loads as a result of the increase in building height from 3 stories to 6 or 12 stories.

1.2.1 Blast Wave

Detonation is a very rapid chemical reaction which has a supersonic velocity. As reaction proceeds through the explosive material, there occurs a shock wave which converts the explosive into hot, a high-pressure gas. The shock wave composed of a high-intensity shock front expands from the point of explosion (UFC 3-340-02). The shock front caused by explosion can be observed from the following photo of the experiment conducted by *Defence Research & Development Canada.*

Figure 1: Image of shock front

Source: Defence Research & Development Canada, date accessed 21.03.16

Needham (2010) defined the blast wave as follows: "The blast wave is characterized by a discontinuous rise at the shock front followed by an immediate decay to a negative phase. The positive phase of a blast wave is usually characterized by the overpressure and is defined as the time between shock arrival and the beginning of the negative phase of the overpressure. The negative phase may asymptotically

approach ambient from below“. The free air burst blast environment can be seen from Figure 2.

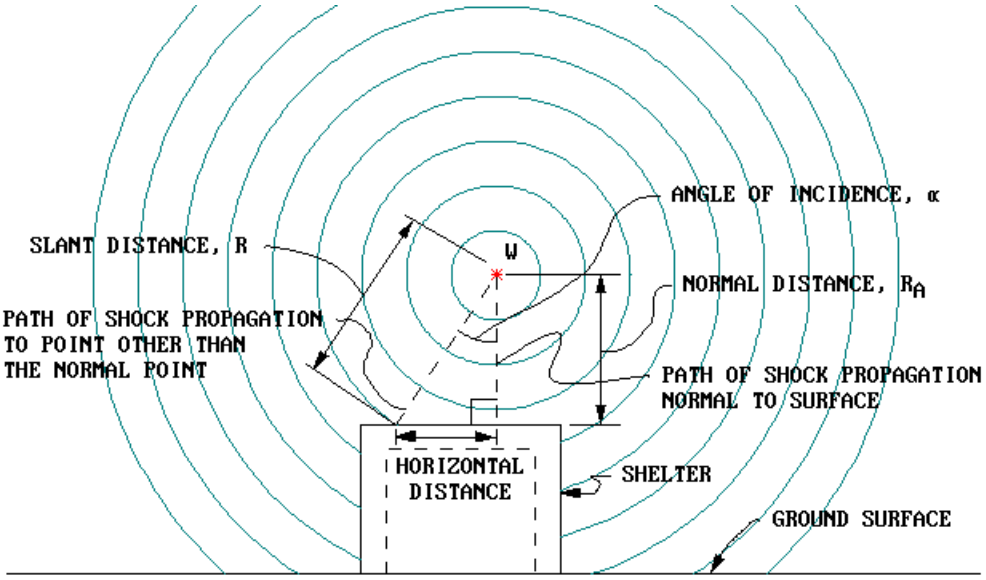

Figure 2: Free air burst blast environment (UFC 3-340-02)

The expansion of the wave results in three subsequent consequences regarding the blast effect: increase in time-interval, reduction in velocity and decrease in the intensity of pressure (UFC 3-340-02/2-8.1).

1.2.2 Pressure Time Profile

The blast wave is comprised of two primary consecutive phases as mentioned, which are respectively the positive and the negative phases. The shock front creates a considerably rapid increase in pressure to the incident or side-on overpressure at arrival time. Consequently, an exponential decay in the incident pressure takes place through the positive phase which results in ambient pressure. The pressure further decreases beyond the ambient pressure which characterizes the negative phase. Moreover, in contrast to the positive phase, lower intensity and longer duration are also characteristics of the negative phase. The ideal blast wave features were provided by Baker (1973) for a spherically symmetric source of explosion taking

place in a homogeneous environment. Figure 3 shows the free field blast pressure profile.

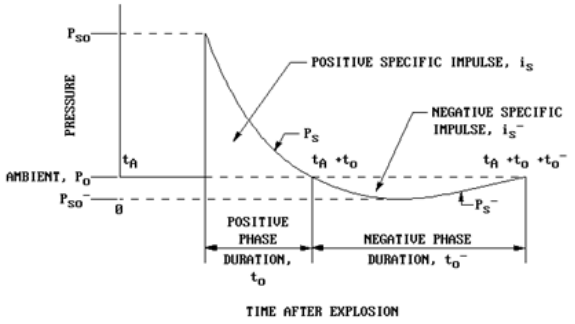

Figure 3: Free-field pressure-time profile (UFC 3-340-02)

The arrival time t_a is directly proportional to the distance between the source of explosion and the observed point, along with the lengthening of the positive phase and the low amplitude side-on overpressure. Alternatively, when the distance decreases, the incidental pressure increases in intensity along with a contraction of the positive phase. The characterization of the pressure in relation to the distance from the source of explosion at particular time intervals is illustrated in Figure 4. A relative vacuum is generated at $t=t_4$ resulting from the expansion of the gases and consequent abrupt decrease in pressure.

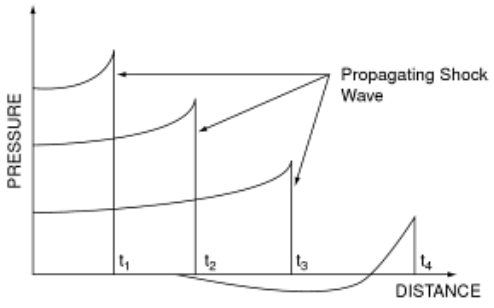

Figure 4: Variation of overpressure in air with distance at successive times

Taking into consideration the fact that blast waves are characterized by velocities greater than that of sound, non-linear equations of motion can be effectively utilized to explain the propagation of blast wave through air. Moreover, various authors in literature have suggested or used practical structures by empirically calibrating these to the measured or predicted time histories, since pressure-time profile can assist in characterizing an ideal blast wave. Generally, many researchers have attempted to prescribe functions regarding pressure time-history *P(t)* of an ideal blast wave concentrating on the positive phase. A decay function in linear form is the simplest function given by the following (Baker, 1973):

$$P(t) = P_0 + P_s\left(1 - \frac{t}{t_d}\right) \tag{1.1}$$

where P_s is the incident pressure, P_0 is the ambient pressure and t_d is the time after the pressure wave arrival.

Dewey, 1964 had suggested to use of modified Friedlander equation that is a function of exponential decay and Baker (1973) had given the function as follows:

$$P(t) = P_0 + P_s^{+}(1 - t/t_d)e^{-\beta t/t_d} \tag{1.2}$$

where β is the decay parameter coefficient.

The most widely used blast wave equation is the modified Friedlander equation. Even though it is not very intricate, it allows the modification to the most important characteristics of the blast wave (Baker, 1973):

$$P(t) = P_0 + P_s\left(1 - \frac{t}{t_d}\right)ac^{-b\frac{t}{t_d}} + (1-a)c^{-c\frac{t}{t_d}} \tag{1.3}$$

In which *a, b* and *c* are constants obtained from experimental data.

It should be duly noted that these equations do not consider the negative phase interval of the blast characterized by lower amplitude. The negative phase duration

has been ignored by most of the researchers. This is owing to either of the two facts: (1) relative insignificance of the negative phase in contrast to the positive phase, or (2) the associated difficulty with the measurement or assessment of the aspects of the negative phase.

An expression for the negative phase pressure is provided in (Baker 1973) in the following form:

$$P(t) = P_0 - P^{-}\left(\frac{t}{t_d^{-}}\right)\left(1-\frac{t}{t_d^{-}}\right)c^{-4\frac{t}{t_d^{-}}} \tag{1.4}$$

where c is a parameter that is obtained from experiments.

1.2.3 Scaling Laws and Scaled Distances

In order to compute the parametric figures of the blast including the positive phase duration, time of arrival, peak pressure and the impulse for the charge weight of interest, empirical methods generally consult reference explosions for comparison and then utilize scaling to reach the required figures (Baker 1973, Baker et al. 1983, Kinney and Graham 1985, Smith and Hetherington 1994).

Sach's scaling (1944) and Hopkinson scaling law (1915) are the most widely scaling laws in blast calculations (Baker, 1973, Baker et al., 1983, Kinney and Graham, 1985). At higher distances from the ground level, Sach's scaling is more effective and thorough for characterizing the blast parameters (Baker et al., 1983). On the other hand, Hopkinson scaling law (Baker et al., 1983) is the more widely utilized scaling law for blast parameters. According to this law, sometimes also referred to as the cube-root scaling law, given two explosions have equal distances on the Z-scale, they will have exactly same parameters for the blast wave. This method defines the scaled distance as:

$$Z = \frac{R}{W^{1/3}} \tag{1.5}$$

where R is the distance between a point of interest and the charge center in meters, and W is the weight of the explosive materials in kilograms.

1.2.4 TNT Equivalence

The specific parameters of the air-blast are determined by the relative distance between the source of explosion and the particular point along with the energy released during the process (Smith and Hetherington, 1994). Taking into consideration the fact that much of the information regarding explosions came about as a result of the invention of TNT and the weight of the charge determining the energy released from the process, the output in terms of equivalent TNT explosive is usually used to measure the parameters for the explosion. Although many methods have been prescribed for the conversion of any explosive mass to its equivalent TNT counterpart, the use of the ratio of combustion heat is the more common and effective method for relating the mass of chemical explosives to the equivalent TNT mass (Henrych, 1979). This is described as:

$$w_{TNT} = \frac{H_{Exp}}{H_{TNT}} w_{Exp} \tag{1.6}$$

where w_{TNT} is the equivalent TNT mass, H_{TNT} is the heat of detonation for TNT, H_{Exp} and w_{Exp} are the heat of combustion and mass of the explosive under consideration respectively.

1.3 Objectives of Research

In this study, the loading during the blast and the material parameters of the affected member were calibrated using the detailed and well-documented experiments conducted by Nassr (2012). Using a finite element model calibrated by using the results of these experiments, the investigation of the effects of both loading parameters and material response were conducted using sensitivity studies. The main objectives of this study can be summarized as follows:

- Understanding the dynamic response of a steel beam-column element response subjected to blast loading,
- Investigation of the effects of the parameters influencing the dynamic behavior of the chosen steel beam-column element,
- Comparison of the characteristics of the blast wave that are calculated by empirical formulas with the experimental data,
- Examination of two different cases of blast response, one undergoing plastic deformation while the other one in the elastic range,
- Investigation of the dynamic response of the chosen system under different blast loading conditions,
- Investigation of the effects of axial loads on the behavior of the chosen element during blast loading.

The aforementioned objectives are going to be carried out using a finite element model whose dynamic behavior is calibrated to the experimental results by Nassr (2012). The general purpose finite element code ABAQUS was utilized for this purpose. Explicit time integration was used during the analyses as the loading times in blast loading are significantly short.

1.4 Blast Load Predictions

Numerical methods are especially practical for the determination of the blast load parameters since they utilize laws characterizing the framework of computational fluid dynamics (CFD) (including equation of state, laws of conservation of mass, energy and momentum). These can alternatively be determined using set of numerical relations that are translated into charts and then imprinted to equations (Lee et al., 2009). These are particularly important since the precise estimation of the space-time distributions of the blast pressure along with its magnitude is very useful in determination of the response of any structure or entity to the blast. The well-known Brode curves (1997) are a result of one such attempt for characterization of the parameters of any blast by Dr. Harold Brode (1955). His equations relate the peak overpressure to the TNT detonation through a spherical charge of TNT. Charlie

Kingery and Gerry Bulmash in 1984 presented a compilation and fit to the measurements of the blast experiments (Kingery &Bulmash, 1984) based on information accumulated and correlated from references to the blast data from various tests accounting up to hundreds of such studies including both reflected case-studies and side-on data. This gave birth to the famous Kingery-Bulmash curves which describe peak overpressure data as a function of the range in the form of an 11^{th} degree polynomial. Furthermore, several other high order polynomial fits are functions of range and describe, amongst other characteristics, the shock velocity, impulse, reflected pressure and the K-B fit for the time of arrival. The widely-famous ConWep, which is an air blast load generation software (Hyde, 1992), is also based on these aforementioned Kingery-Bulmash equations (also known as the air blast parameter equations). However, the ConWep along with the famous endeavors of Kingery and Bulmash can only be accessed by government contractors and US military personnel and hence its distribution is severely limited.

1.4.1 Peak Overpressure

The works of Smith and Hetherington (1994) and Kinney and Graham (1985) include alternative equations for air blast parameters, but do not include complete information about peak values of shock overpressure P_s, as taken from Brode, 1977.

$$P_s = {}^{6.7}/_{Z^3} + 1, \qquad P_s > 10\ bar \tag{1.7}$$

$$P_s = {}^{0.975}/_{Z} + {}^{1.455}/_{Z^2} + {}^{5.850}/_{Z^3} - 0.019\ , \qquad 0.1 < P_s < 10\ bar \tag{1.8}$$

1.4.2 Positive and Negative Impulses

As aforementioned, the two phases characterize the blast loading profile: the positive phase with time interval t_d is the area above the ambient pressure while in contrast, the negative phase with time interval $\bar{t_d}$ is the area below the ambient pressure.

Another primary parameter of the pressure time profile is the impulse. *I* is the impulse taking place in the positive phase and is calculated as the portion underneath the pressure time curve from arrival time t_a to the commencement of the positive phase (Baker et al. 1983). This is described as:

$$I^{+} = \int_{t_a}^{t_a+t_d} P(t)dt \tag{1.9}$$

Similarly, the negative impulse can be given as (Baker et al. 1983)

$$I^{-} = \int_{t_a+t_d}^{t_a+t_d+\bar{t}_d} P(t)dt \tag{1.10}$$

1.4.3 Positive Phase Duration 't_d'

Even though the results of Smith and Hetherington (1994) and Kinney and Graham (1985) do not take the comprehensive information regarding peak values of shock overpressure P_s into account, they do include alternative models for various parameters of the air blast. The duration of the positive phase (t_d) in milliseconds (ms) is described (Kinney and Graham, 1985) as:

$$\frac{t_d}{W} = \frac{980\left[1+\left(\frac{Z}{0.54}\right)^{10}\right]}{\left[1+\left(\frac{Z}{0.02}\right)^{3}\right]+\left[1+\left(\frac{Z}{0.74}\right)^{6}\right]+\left[1+\left(\frac{Z}{6.9}\right)^{2}\right]} \tag{1.11}$$

1.4.4 Arrival Time 't_a'

Neither Kinney and Graham (1985) nor Brode (1977) assist in the matter of determination of an appropriate formulation regarding the arrival time.

The formulation of equations expressing arrival time was achieved using conclusions from 1 kg TNT reference explosion from Kinney and Graham (1985). Utilizing piece-wise fitting of polynomials, the resulting polynomial for arrival time is described as:

$$\frac{t_a}{W^{1/3}} = \sum_{i=1}^{4} a_i Z^{i-1}, 0.3 \leq Z \leq 500\, m/kg^{1/3} \quad (1.12)$$

where t_a is the arrival time, in seconds, of the shock wave.

For various ranges of scaled distance *Z*, the values of the fitted polynomial coefficients a_i are included Table 1.

Table 1: Fitted polynomial coefficients to define the arrival time (United Nations Office for Disarmament Affairs,2013)

Range (m/kg$^{1/3}$)	a_0	a_1	a_2	a_3
0.3 ≤ Z < 2.4	1,769362E-02	-2,032568E-02	5,395856E-01	-3,010011E-02
2.4 ≤ Z < 12	-2,251244E+00	1,765820E+00	1,140477E-01	-4,066734E-03
12 ≤ Z ≤ 500	-6,852501E+00	2,907447E+00	2,907447E+00	-9,344539E-08

1.5 Blast Structure Interaction

Under the situation that an entity is obstructing the path of an expanding blast wave, the air circumvents the structure. This results in the blast loading surrounding the entity which is entirely dependent on the topology and dimensions of the object. Moreover, the characteristics of the explosive determine the distribution and amount of the structural loading, where the source of the explosion relative to the structure along with the angle of incidence are the most important factors (Baker et. al. 1983; Smith and Hetherington 1994; USDOD 2008). Substantial alteration in the energy released occurs depending upon the explosive material and the weight along with the pressure being exerted on the entity which is dependent upon the size of the explosion. The fact that should be noted is that the impact of the air burst is different

from the surface burst. This is due to the fact that as it comes into contact with other structures with are denser compared to air, alteration in its magnitude takes place with reflected pressure being magnified.

1.5.1 Dynamic Pressure

Apart from the peak overpressure, 'dynamic pressure' is another property which quantifies the destructive effects of any blast wave (Smith and Hetherington, 1994). The air behind the shock front is moving outward at a lower velocity owing to the propagation of the blast wave through the environment. There is a direct relation between dynamic pressure and the square of the wind velocity as well as the density of the air behind the shock front. (Glasstone and Dolan, 1977). The peak overpressure determines the velocity of the air and consequently the wind pressure, which is also related to the aforementioned dynamic pressure *q(t).* Both velocity of blast wave and dynamic pressure are highly dependent on incident pressure (Rankine and Hugoniot, 1870). The velocity of wave front U_s was given as (Rankine and Hugoniot, 1870)

$$U_s = \sqrt{\frac{6p_s + 7p_0}{7p_0}} \cdot a_0 \tag{1.13}$$

where P_s is the overpressure, P_0 is the ambient of air pressure, a_o is the speed of the sound in the air.

The drag force in relation to the solid winds of the passage of the blast wave determines the level of blast loading for numerous kinds of building forms. Although the drag force is dependent upon the highest figure for the dynamic pressure (peak overpressure) along with its duration at a particular location, the deterministic attributes also include topology and size of the structure. R-H equations characterize the combinations of the conservation equations across a shock. In other words, the expressions for conservation of energy, momentum and mass across the shock front are the Rankine-Hugoniot relations. Equation (1.14) describes the Rankine-Hugoniot relation regarding the dynamic pressure *q*.

$$q = \frac{P_S^2}{[2\gamma P_0 + (\gamma - 1)P_S]} \tag{1.14}$$

Incident pressure P_s, ambient pressure P_o, and specific heat ratio γ are the three variables which determine the dynamic pressure q.

The ratio of the specific heat keeping the volume constant gives the figure for γ. Although air is a mixture of various gases, the assumption of air being an ideal gas with gamma value of 1.4 is a considerably good approximation for many practical purposes. However, the limitations for this assumption must also be taken into account. The γ commences to deviate from this value when the incident pressure exceeds 20 bars.

Equation (1.15) mathematically represents the resultant reflected overpressure at the shock front as a result of a shock wave striking a solid surface, when the velocity vector is perpendicular to it.

$$P_r = 2P_s + (\gamma + 1)q \tag{1.15}$$

There is an inverse relation between the peak dynamic pressure and distance from the explosion center just like the peak shock overpressure; however, the difference in rates exists.

The maximum value q_s, is given by Rankine and Hugoniot (1870) as

$$q_s = \frac{5p_s^2}{2(p_s + 7p_0)} \tag{1.16}$$

where P_s is the overpressure, P_0 is the ambient of air pressure and q_s is the dynamic pressure.

1.5.2 Reflected Blast Wave

The shock wave faces an abrupt stop when it comes in contact with a solid surface (building). The pressure increases dramatically as compared to the pressure in the incident blast wave. This sudden magnification of blast wave is known as reflection. The maximum load on blast loaded structure is produced by reflected pressure P_r, which is why a structure cannot be properly designed without the proper knowledge of the reflection phenomenon.

The air molecules involved in the reflection process come to rest, facing a momentum change with the surface. The molecular effect is then transferred to the layer behind, and the momentum thus produced in the second layer of air, compresses the first layer even more. The effect is then transferred to all the succeeding layers and reflected pressure P_r is thus produced. In other words, the incident pressure when combined with the dynamic pressure of the blast in relation to the velocity of the air molecules produces the reflected pressure P_r.

The reflected pressure does not equal to the direct summation of the incident pressure and the dynamic pressure, because momentum change of the air and its increased compression also act as contributing factors. It is given the name of blast loading on the structure because it is the sum of all pressure applied on the surface under consideration. The peak incident pressure P_s is amplified by reflection factor, when it comes in contact with a structure in its propagation pathway. Reflection coefficient Cr_a is a measure which is the ratio of pressure being exerted on the surface of the object in comparison to the incident pressure and is also dependent on the angle of the incident pressure α_i.

Depending on the type of reflection, reflection factors take different values. There are three basic types of reflection of a shock plane which are: Normal reflection of a shock plane from rigid wall, Regular oblique reflection of a shock plane from a rigid wall and Mach reflection from a rigid wall.

It is important to note that for any given strength of incident shock there is a corresponding critical angle of incidence α_{Icrit}. A shock wave cannot be reflected at angle larger than its critical angle. The reflected pressure coefficients for different incident overpressure values can be observed from the Figure 5 according to the angle of incidence.

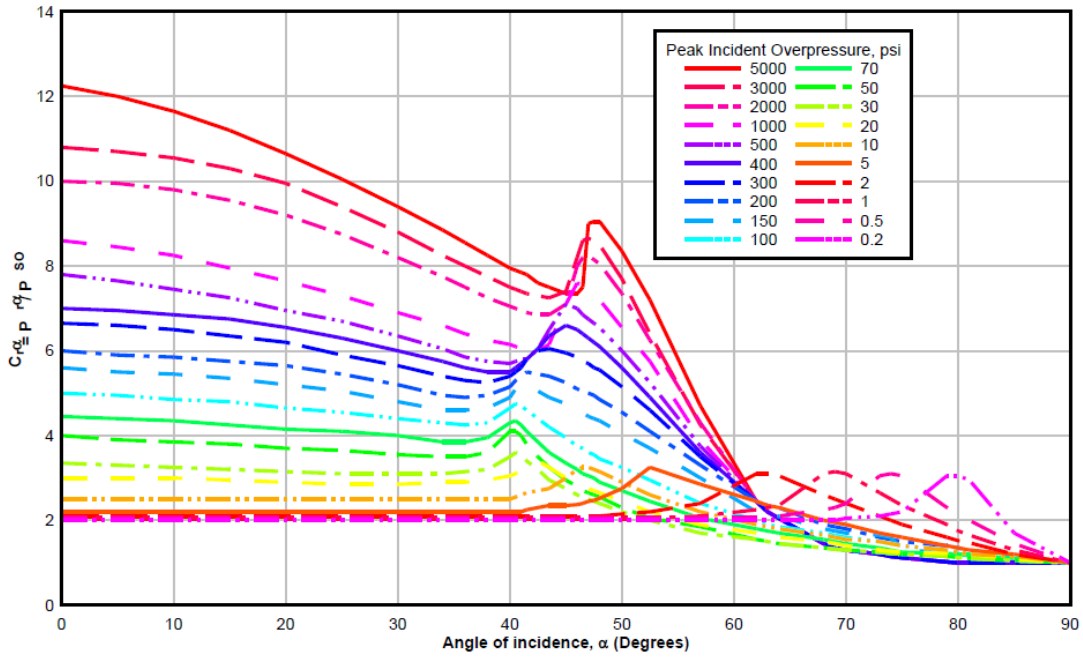

Figure 5: Reflected pressure Coefficient versus angle of Incidence (UFC 3-340-02)

The reflected pressure caused by a surface burst with an angle of incidence equal to 0 degree can be given as example for 'normal reflection of a shock plane from rigid wall' type of reflection. On the other hand, as the angle of incidence increases, the reflection factors decrease, resulting in relatively small reflected pressure. This case can be considered as 'regular oblique reflection of a shock plane from a rigid wall'.

Depending on the location of detonations with respect to the ground surface, the reflected pressure wave show variety. The following figure (Figure 6) shows the air burst blast environment caused by explosion that occur above the ground surface.

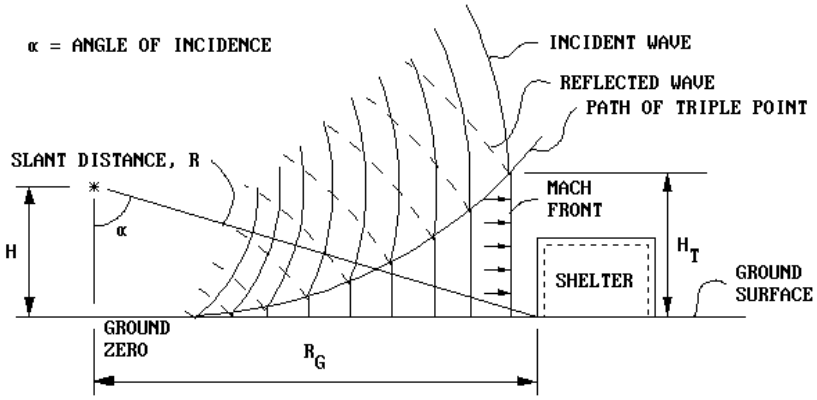

Figure 6: Air burst blast environment (UFC 3-340-02)

The pressure reflected from ground surface coincides with the incident pressure and form a front named as Mach front. This is the most complex type of reflection and used in Second World War to increase the nuclear weapon effect. (UFC 3-340-02; Eichinger, 1985)

The surface bursts which occur on the ground surface produce reflected wave at very initial stage of the explosion. The ground reinforces the blast wave at the point of the detonation (UFC 3-340-02). The surface burst blast environment is given in Figure 7.

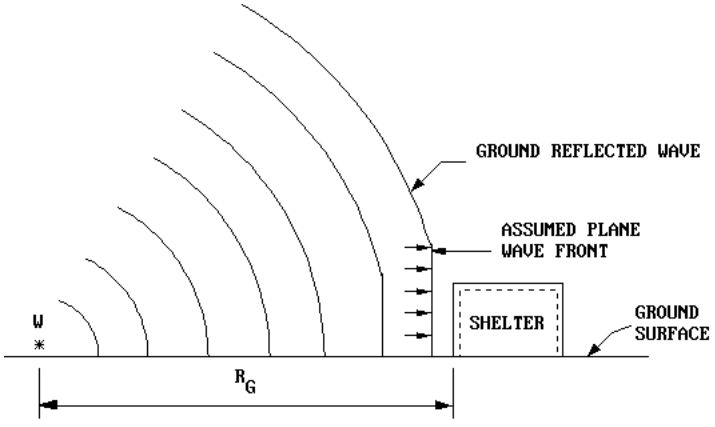

Figure 7: Surface burst blast environment (UFC 3-340-02)

1.5.3 Reflected Pressure Predictions

Bogosian et al. (2002) classified the available air blast data into reflected and incident blast parameters in a tabular form. This tabulation of the raw air blast database showed similar trends in the reflected and incident overpressure measurements. However, it is rather difficult to estimate peak reflected overpressure P_r in such data sets. The sources that included parameter information for reflected overpressures do so on the basis of normally reflected case and the effects of angle of incidence are mentioned separately.

As mentioned before, Rankine and Hugoniot suggested equations to calculate dynamic pressure and wave front velocity to examine the nature of reflected pressure. Rankine and Hugoniot also derived the equation for reflected overpressure P_r as follows

$$p_r = 2p_s\left[\frac{7p_0 + 4p_s}{7p_0 + 7p_s}\right] \text{ (Army TM5-1300, Navy NAVFAC)} \qquad (1.17)$$

where P_r is the maximum overpressure for normal reflection, P_s is the peak side-on overpressure and P_0 is the ambient air pressure.

Air is considered an ideal gas to be able to establish a relation between peak side-on overpressure and peak reflected overpressure (Brode, 1977). Equation (1.18) is recommended by Brode for explosions having side-on overpressure lower than 6.9 bar for the calculation of the peak reflected overpressure.

$$P_r = P_s\left(2 + \frac{6P_s}{P_s + 7P_0}\right) \qquad P_r<6.9 \text{ bar} \qquad (1.18)$$

where P_r is the maximum overpressure for normal reflection, P_s is the peak side-on overpressure and P_0 is the ambient air pressure. It is assumed that the heat capacity ratio of the air medium is equal to 1.4.

However, when the overpressure of the air is more than 6.9 bars, air cannot be considered an ideal gas anymore as the molecules begin to interact with each other. For this special situation Brode recommends Equation (1.19) for the calculation of peak normally reflected overpressure.

$$P_r = P_s\left(\frac{0.03851P_S}{1+0.0025061P_S+4.041\times10^{-7}P_S^2}+2+\frac{0.004218+0.7011P_S+0.001442P_S^2}{1+0.1160P_S+8.086\times10^{-4}P_S^2}\right) \tag{1.19}$$

The semi-empirical equation expressed below was proposed by Kinney and Graham (1985) for determination of the reflected pressure P_r in kPa

$$P_r = 2P_s\left(\frac{7P_0+4P_s}{7P_0+P_s}\right) \tag{1.20}$$

in which P_o is the atmospheric pressure and P_s is the incident overpressure.
The incident overpressure P_s is given in terms of Z in Equation (1.21) (Kinney and Graham, 1985).

$$\frac{P_s}{P_0} = \frac{808\left[1+\left(\frac{Z}{4.5}\right)^2\right]}{\sqrt{1+\left(\frac{Z}{0.048}\right)^2}\sqrt{1+\left(\frac{Z}{0.74}\right)^2}\sqrt{1+\left(\frac{Z}{1.35}\right)^2}} \tag{1.21}$$

In Equation (1.9), the suggested positive impulse equation has been covered. Following equation expresses the positive reflected impulse I_r in kPa by Prugh (1999).

$$\frac{I_r}{W^{1/3}} = 8.97\left(\frac{200}{Z^{1.5}}+\frac{125}{Z}\right) \tag{1.22}$$

1.5.4 Strain Rate Effect

The effects of various strain rates on the dynamic features of different materials that are subjected to dynamic loads have been extensively studied and published for future referencing by large number of researchers. According to these studies there is a strong correlation between the strain rate and the strength of the material. The strain rate strongly effects the inelastic deformation, which is a consequence of some shock or impact event. Most materials' strength increases with the increase in the strain rate. In the representation of the high-energy dynamic events, this effect is considered very significant. Although the effect of this phenomenon can be considered as advantageous, there is a chance of obtaining somewhat larger deformations due to the structural resistance against change of mode (Jones, 1988).

K. T. Ramesh (2008) stated that the strain rates below 10^{-3} s^{-1} are experienced in the quasi-static deformation and the experienced strain rate that is above 10^{2} s^{-1} is called as high strain rate. On the other hand, strain rates above 10^{4} s^{-1} are classified as very high strain rates and the strain rates above 10^{6} s^{-1} are classified as ultra-high strain rates. In order to investigate the response of different steel types (used in automobile industry) to different strain rates, Gao et al. (2015) studied steel types classified as TRIP A, TRIP B and DP A. In this study, the yield strength of steels TRIP A, TRIP B and DP A at a strain rate 10^{-1} s^{-1} increased by about 8%, 9% and 4% with respect to loading at a strain rate of 10^{-4} s^{-1}. At a strain rate 10^{2} s^{-1}, the yield strength of steels TRIP A, TRIP B and DP A increased significantly more, by about 38%, 24% and 4% with respect to results from the loading at strain rates of 10^{-4} s^{-1}. The experiment conducted by G. H. Majzoobi et al. (2016) to investigate the change in yield stress of HSLA steel subjected to loading at different strain rates showed that at the room temperature if the strain rate increased to 350 s^{-1} , the change in yield stress was about 30%. On the other hand, as the strain rate increased to 1600 s^{-1} and 5400 s^{-1}, the change in yield stress was obtained at 48% and 63%, respectively.

The strain rate effect is also determined to be an independent phenomenon of structural geometry by Jones (1988). No correlation was found between the carbon content of steel and the material strain rate sensitivity according to Itabashi and Kawata (1999). Johnson-Cook plasticity was used to represent the strain rate effect in this study, utilizing the Johnson-Cook isotropic hardening model as explained below.

1.5.5 Johnson-Cook Plasticity

Among all the developed models of material plasticity, Johnson-Cook plasticity model (Johnson and Cook, 1983&1985) is the perhaps the most pragmatic, particularly in the context of high-strain-rate deformation of metals. Inclusion of the hardening law and the rate dependence in the design makes it a special type of von-Mises plasticity model. Johnson-Cook hardening is a unique model of isotropic hardening as the yield surface is expressed as a mathematical function of the corresponding plastic strain, strain rate and the temperature.

$$\sigma_Y = \left[A + B\left(\varepsilon_{eff}^{p}\right)^{n}\right](1 + C \ln \dot{\varepsilon})[1 - (T_H)^{M}] \tag{1.23}$$

where;

ε_{eff}^{p} = effective plastic strain

$\dot{\varepsilon} = \frac{\dot{\varepsilon}_{eff}^{p}}{\dot{\varepsilon}_0}$ where $\dot{\varepsilon}_0$ is strain rate used to determine A, B & n

$T_H = \frac{T - T_R}{T_M - T_R}$ homologous temperature

$T_M =$ melt temperature

$T_R =$ reference temperature when determining A, B & n

The expression in the first set of brackets gives the stress as a function of strain. The expressions in the second and third set of brackets represent the strain rate effect and temperature softening, respectively.

CHAPTER 2

VALIDATION OF ABAQUS MODEL WITH EXPERIMENTAL RESULTS

In this chapter, the response of beam-column elements to blast loading is investigated using parametric studies in order to determine the effect of the simulation choices on the predicted response. For this purpose, initially, the dynamic constitutive material properties of the Johnson-Cook constitutive model were calibrated using the experimental response of the two different steel beam-column elements that are subjected to blast loading. The chapter is organized in the following fashion. First, the experiments (including the test matrix, test setup and instrumentation) that are carried out by Nassr et. al. (2012) on beam-column elements subjected to blast loading are presented. Not only the reflected pressures, impulses and positive phase durations that are measured by different transducers along with the strain time histories and displacement time histories of the test columns measured by strain gauges are presented. Secondly, the initial values that are used in the calibration process to determine most accurate and reliable Johnson-Cook constitutive model parameters are given. Thirdly, the results of the calibrated model and the parametric studies will be mentioned. Parametric studies are performed in order to observe the effects of the five material constants of Johnson-Cook Plasticity model. Finally, the dynamic response of the steel beam-column under different blast loading conditions will be presented.

2.1 "Experimental Performance of Steel Beams under Blast Loading "(Nassr et al. 2012)

Nassr et al. (2012) have evaluated the dynamic response of wide-flange steel beams and columns to blast loading by conducting experiments with explosives. The blast shots that are generated by different combination of stand-off distance and charge weight are examined on different section sizes.

2.1.1 Experimental Setup of Nassr's Research

In the following sections the test matrix, test setup and the information about instrumentation used by Nassr et al. is presented.

Test matrix

Each column was subjected to one of five blast shots generated by different combinations of charge weight and stand-off distance, as shown in Table 2.

Table 2: Matrix of Test Specimens (Nassr, 2012)

Shot	Section Designation	Axial Load (P) (kN)	Weigth of Charge (kg)	Stand-off Distance (m)	Scaled Distance (m/kg)	Test Columns
1	W150X24	270	50	10.30	2.8	1C1, 1C2, 1C3
2	W150X24	270	100	10.30	2.22	2C1, 2C2, 2C3
3	W150X24	270	150	9.00	1.69	3C1, 3C2, 3C3
4	W150X24	270	250	7.00	1.11	4C1, 4C2, 4C3
5	W200X71	640	250	9.50	1.51	5C1

All the blast shots were conducted in the field, where the maximum charge size used was limited to 250 kg of ANFO (ammonium nitrate/fuel oil). It is worth mentioning that extremely high pressures can be achieved by close-in explosions involving small charges, but such blast-scenarios would result in local failure modes, such as breaching and tearing, that were not intended to be the focus of the testing programme with the goal of investigating the behavior of full size column specimens subjected to plane shock waves and essentially uniform pressure. The ground stand-off distance ranged from 7 m to 10.3 m while the charge size varied from 50 to 250

kg. A total of twelve W150X24 section columns were tested in shots 1 to 4 had while one W200X71 section column was tested in shot 5.

Test Specimens

Two sections W150X24 and W200X71 that are often used in low-moderate rise steel buildings were chosen for the experimental study. Thirteen specimens (each having a height of 2413 mm), were tested using explosive charges. The ultimate strength and yield stress of W200×71 section were 474 and 362 MPa and those of W150×24 section were 537 and 393 MPa, respectively.

In order to create a static axial load on a section, the columns of the size W150×24 was pre-strained in an axis through two 7-wire pre-strained strands with a nominal ultimate tensile strength of 1860 MPa and a diameter of 13mm. To create a static axial load on the column with size W200X71 section, the axial load was applied by four 13 mm diameter symmetrically pre-strained strands. These cables were set firmly on thick steel plate connected to each end of the column of thickness 24.5mm. The cables were then put through tensile stress at the same time, with an axial force of 25% of the static axial load capacity the column. The pre-strained strands were fixed at a medium height of the cross-section for the circumvention of the extension of lateral vibration in order to reduce the variation on axial load.

Test Setup

The front-facing and the side angles of the setups 1 to 4 in the trial program are shown in Figure 8. The frame sustaining the columns were made up of two RC beams and the columns were intersecting each other at the 4 edges through the steel sockets built into them.

Figure 8: Front and side views of test setup (Nassr, 2012)

An ISO steel container was placed behind the frame so that the specimens are confined and do not engulfed by the shock wave. This wrap around occurrence must be avoided as it has a dominating consequence on the pressure and impulse. The container sheltered the wiring and instrumentation from the effects of the blast. There were also some plywood panels added to the boundary wrap up that were placed between the tests specimens to secure them from the shock and pressure of the blasts.

A totally reflecting plane with a size almost equal to 5.42×3.72 m was produced by the concrete block wing walls (shown in Figure 8) that was placed around the RC frame firmly as shown in Figure 9. This type of arrangement yields a uniform peak of pressure and the impulse on the specimen columns by the reduction of the clearing effect. According to Smith and Hetherington (1994), the clearing effect occurs due to the rarefaction waves travelling back and forth from the boundaries of the reflecting surface and creates a pressure, which then reduces the sum of the specific impulse. Figure 9 shows a detailed test setup having all the important apparatus that includes the frame dimensions, dimensions of the overall reflecting surface, and column spacing.

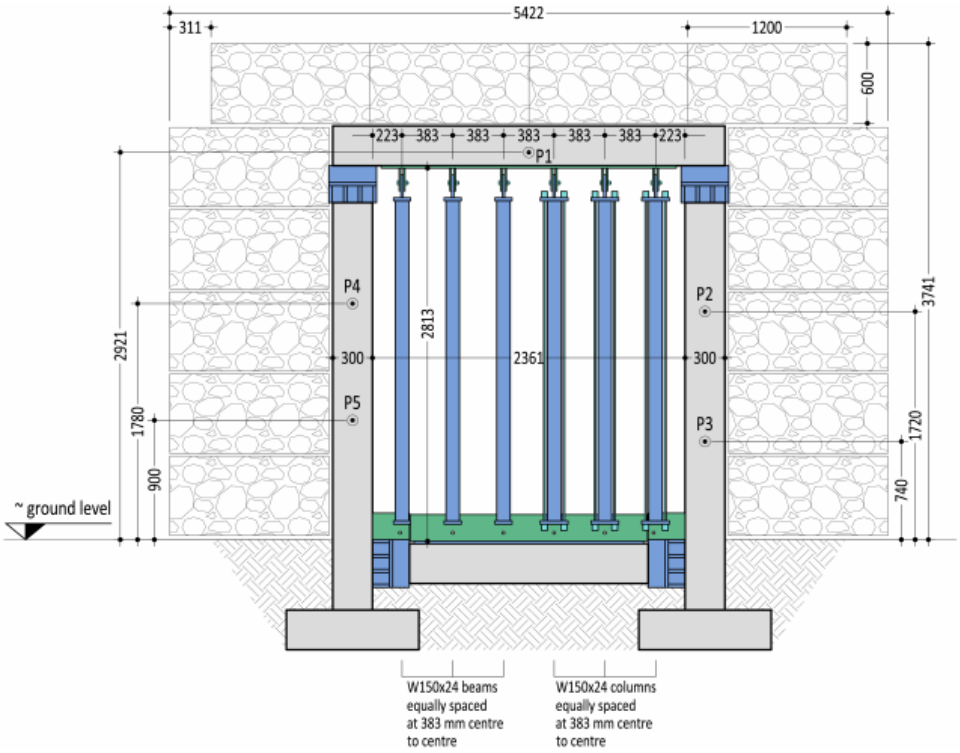

Figure 9: Dimensions of the reflecting surface (in mm) (Nassr, 2012)

The apparatus was used for shots 1 to 4, with each shot involving the testing of six W150×24 members, each of which were 3 beams and 3 columns. In order to provide a steady pressure field on the test specimen, a ground standoff distance of 9.5 m was selected for the column having W200X71 section, which resulted in a scaled distance of 1.51 m/kg$^{1/3}$. The reflected pressure for the selected distance acting on the surface of the column facing towards the blast was not considered enough to produce an acceptably high stress in the column. Consequently, the blast load acting on column was increased by placing the steel curtain which had 1.18 m width and 2.50 m height. The curtain included twelve 1180 mm long structural steel elements built from HSS 254×152×6.4 mm sections. This curtain was designed so as to increase the blast load on the column by shifting the blast pressure that was put on the plane towards the flange of the column. This curtain was supported by a roller at the end and steel columns were fixed at the top. The top of the column was fixed to the RC frame through steel bolts. A gap of 100 mm was left between the bottom end of every column and the support frame for unlimited axial displacement. A round slab

was fixed at the end of the columns and a bar acting against the set was fixed to the end of the frame, supporting it to sustain the roller. A steel shackle was also attached to the end of the column so that the column could swing freely in between the negative or rebound phase of the motion.

Instrumentation

The instrumentation layout for the test setup is presented in Figure 10. As the test program induced damage to the numerous displacement potentiometers, only the mid-span displacement potentiometer was used in which the transducers D-3C1 and D-2C1 were used to record the time history for columns 3C1 and 2C1 respectively. Moreover as illustrated in Figure 10, the strain time-history was captured at several points along each column by using 120 ohm strain gauges. The variation of strain along the span and over the cross-section was captured by various strain gauge arrangements, as depicted in figure below.

According to the specific arrangement in Figure 10, a designation was given to each strain gauge indicating the shot number and its location, e.g. the designation 3-SC6 was given to the results obtained from the strain gauge 6 for shot 3.

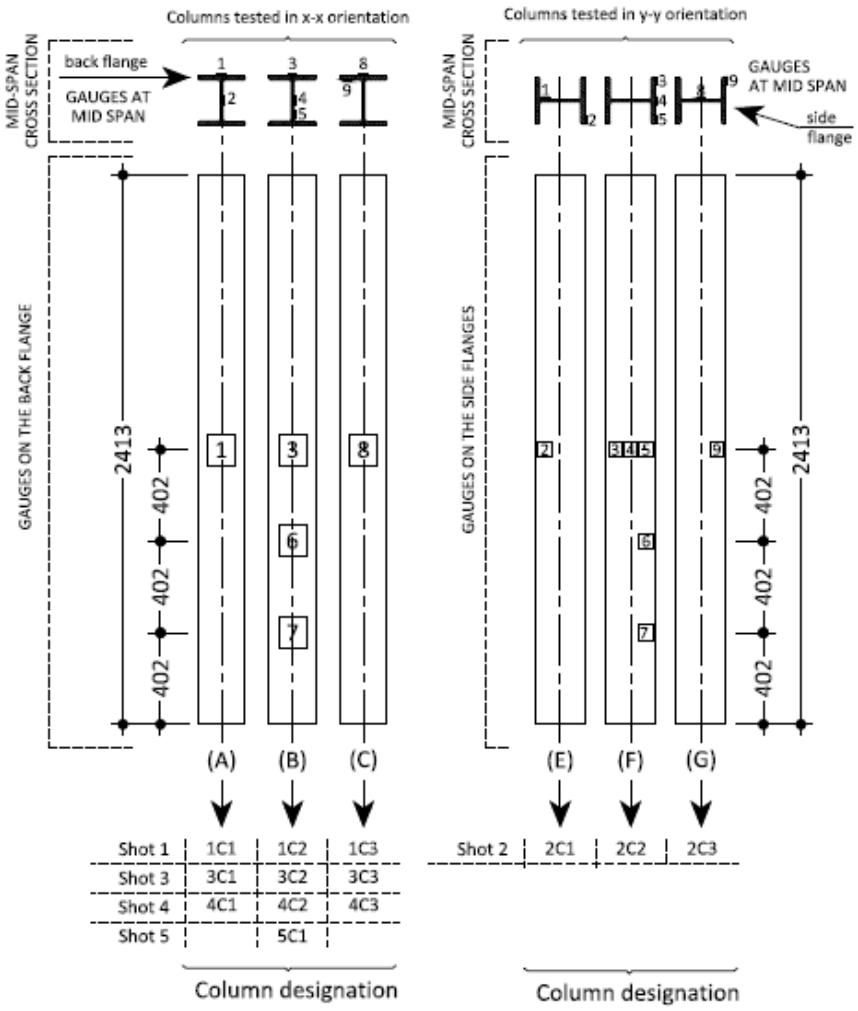

Figure 10: The strain gauge layout (Nassr, 2012)

2.1.2 Experimental Results of Nassr's Research

In this section of the study, the results of two different section sizes W150x24 and W200x71 each with span length of 2413 mm, which were depicted as 3C1 and 5C1, respectively, (Nassr, 2012) were presented. These results were used for the validation of the modeling process in ABAQUS/CAE. The computational models were calibrated according to these test results conducted on these two steel beam-column elements.

The static nominal yield stress and ultimate strength of each section is tabulated in Table 3.

Table 3: Strength characteristics of sections

Section Size	*Yield Stress Mpa*	*Ultimate Strength Mpa*
W150x24	393	537
W200x71	362	474

In order to achieve different levels of dynamic response, different scaled distances and charge weights were used in the experiment. To investigate the dynamic response of W150x24 section, five steel elements were tested with 150 kg ANFO explosives with 9.0 meters stand-off distance. The axial load was 270 kN which is the 25% of axial capacity of these elements. The section W150x24 experienced only elastic deformations: no permanent deformations were observed in either in-plane or the out-of-plane directions. The maximum displacement observed was 30.9 mm and maximum strain was 1500 με for the case with axial loading. The strain-time and displacement-time histories for this specimen are presented in Figure 11.

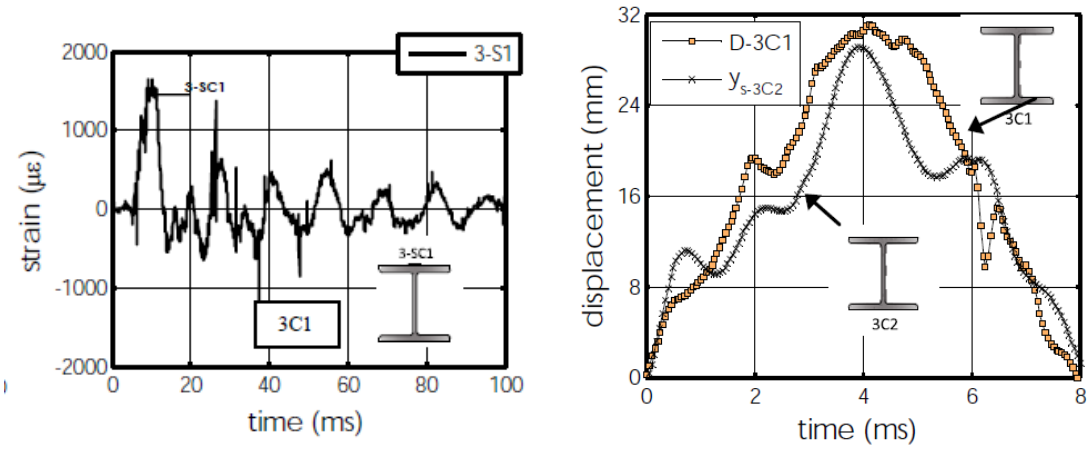

Figure 11: Strain-time and displacement-time histories at mid-span flange surface of 3C1 (Nassr, 2012)

In order to investigate the dynamic response of W200x71 section to the blast loading, five steel elements were tested with 250 kg ANFO explosives with 9.5 meters stand-off distance. The axial load was 640 kN on these elements throughout the test. The steel beam-columns were axially loaded by 25% of axial load capacity of these elements. The section experienced a peak permanent deformation of 32.8 mm at the mid-span. Maximum deformation was observed as 71 mm while the maximum strain was 3842 με for the case with axial loading. Because of the effect of the blast, the displacement transducer D-5C1 could not record the displacement-time history of shot 5 for the column 1. The provided displacement time history of this column in Figure 12 was obtained by integrating the strain–time history of the related column by Nassr et al. (2012). (This integrated curvature was named as '$y_{s\text{-}5C1}$' in this study)

On the other hand, when the axial load was not present, the maximum displacement, maximum permanent deformation and the maximum strain were obtained as 62.8 mm, 30.7 mm and 2536 με, respectively. The peak reflected pressure was recorded as 2098 kPa. The average of the maximum measured tensile strains was 1880 με. Moreover, the recorded maximum compressive strain was 1600 με in the mid-span web- flange connection point. The strain-time and displacement-time histories for this specimen are presented in Figure 12.

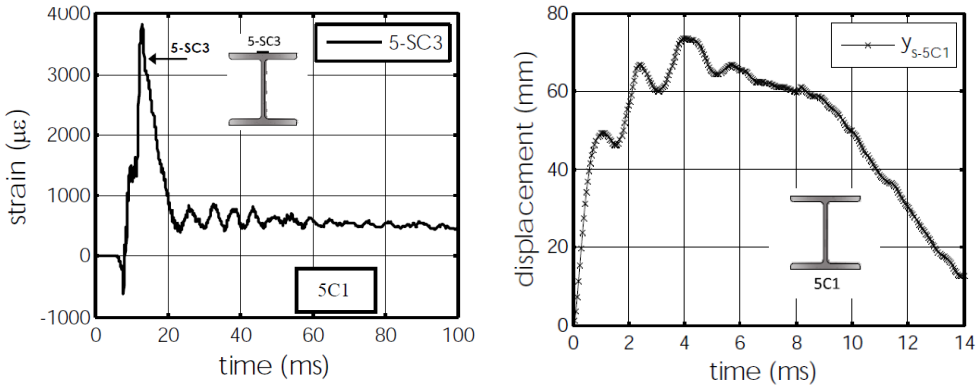

Figure 12: Strain-time and displacement-time histories at mid-span flange surface of 5C1 (Nassr, 2012)

2.2 ABAQUS Finite Element Model

The general purpose finite element program ABAQUS/CAE was used in this study. The calibration of the ABAQUS models was conducted for the aforementioned specimens. Information about the finite element models used in this study are presented as follows.

2.2.1 Finite Element Mesh

The FEM software ABAQUS/CAE was used in this research to analyze steel beam-columns and to compare its results with those obtained from Nassr's experimental research. Not only has the very short duration of the loading, but also the very large overpressure necessitated the use of explicit dynamic analysis to investigate the effect of blast phenomenon on steel beam-column elements. Finite element models used in this study are detailed models of the specimens utilizing solid elements. In order to represent the experimental setup and to restrain the warping effect of the elements, two rigid plates having a thickness of 24 mm were modeled at each end of the steel beam-column elements. Other constituents of the testing program were not included in the model and the tests were represented by the loading on the modeled specimens.

ABAQUS/CAE can utilize various finite elements for the solution of complicated mechanical problems including first-order, reduced integration, solid elements that can be in form of 4 node quadrilaterals, 3 node triangles, 8 node hexahedra or 4 node tetrahedrals. Eight-node linear hexahedron solid elements with reduced integration was used in this study to model the specimens. The three-dimensional model of the 2413 mm long steel beam-column '3C1' is shown in Figure 13. The column was modelled with 5462 nodes and 2904 eight-node elements while the rigid plates at each end were modelled with 40 eight-node reduced integration hexahedron solids. Furthermore one of the rigid plates was pin-supported while a roller was placed on the horizontal centerline of the other one at the external surface.

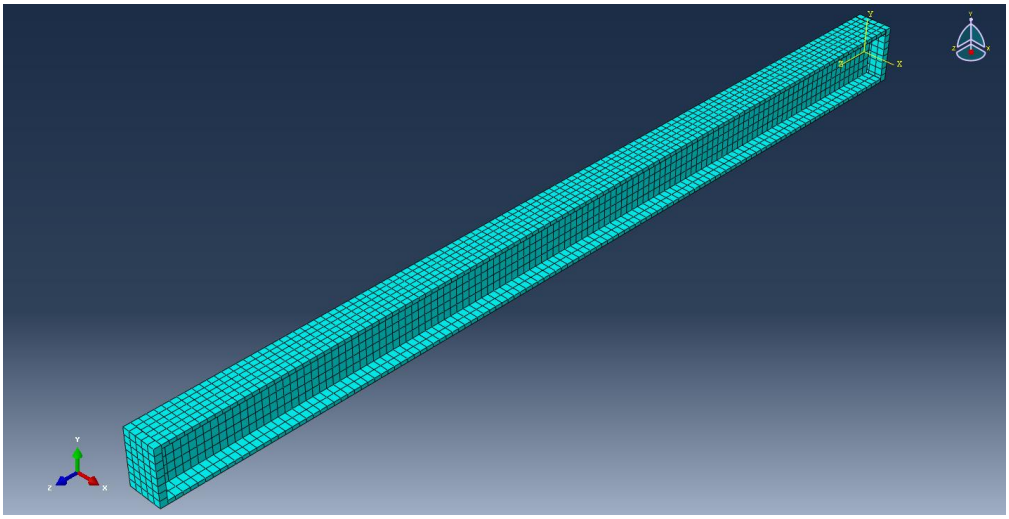

Figure 13: Finite Element Mesh of Section W150x24 – 3C1

The beam-column ‘5C1’ was modeled using 16452 nodes and 8533 eight-node linear solid elements while the rigid end plates were modelled by using 196 eight-node solids. As before, one of the rigid plates was pin-supported while a roller was placed on the horizontal centerline of the other one at the external surface. The finite element mesh of 5C1 is presented in Figure 14.

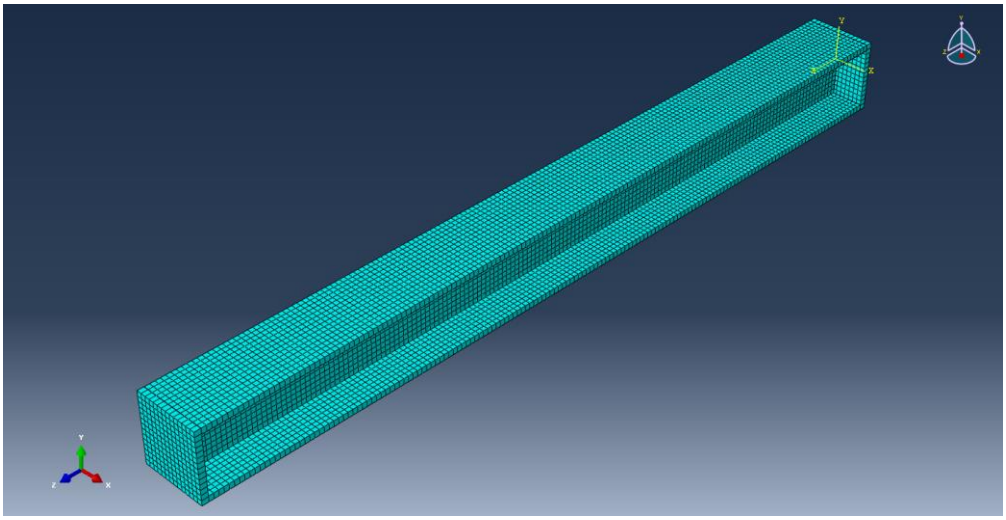

Figure 14: Finite Element Mesh of Section W200x71 - 5C1

The boundary conditions for the models were set as follows: At the hinge end all the translations and rotations were restrained with the exception of the rotation about x-axis. On the other hand, at the roller supported end, other than the rotation around x-axis and translation in the z-direction, all of the translations and rotations are prevented. The associated boundary conditions for the steel beam column elements is shown in Figure 15.

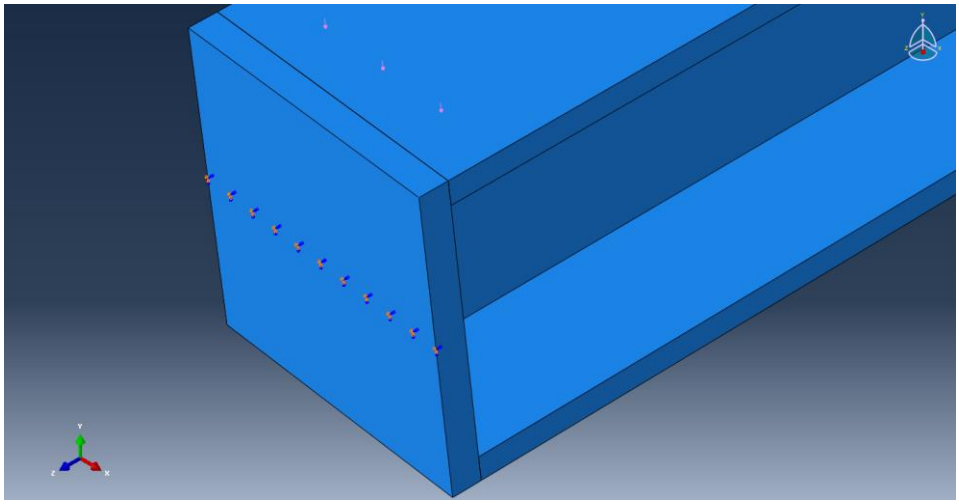

Figure 15: Boundary Conditions of 3C1

2.2.2 Loading Properties

The study of Nassr presented the positive phase data such as reflected pressure P_r, reflected impulses I_r and positive phase durationt_d. The experimental data on the reflected pressure for the test shot 3 is provided in Table 4. It can be seen from the data in Table 4 that the mean value for P_r was 1.560 MPa and maximum measured reflected pressure is 27% higher than the mean value. The measured positive phase duration, t_d, had a varying characteristics. Although, the positive phase duration mean value was 6.2 ms, the measured minimum positive phase duration value is 4.9 ms which is 21% lesser than the mean value.

Table 4: Recorded reflected pressure data for test shot 3

	td (ms)	Pr (Mpa)	Ir (Mpa.ms)
Point 1	6.7	1.293	1.877
Point 2	6.8	1.409	1.765
Point 3	6.1	1.484	2.688
Point 4	6.3	1.984	2.250
Point 5	4.9	1.631	2.058
Mean Value	6.2	1.560	2.128

The table below illustrates the reflected impulses that had been obtained from experiment that was conducted for shot 5 (Nassr, 2012). The point 2 data are not available because of the destruction of the transducer at that point. As can be seen from the Table 5, the mean value of the reflected impulse is 2.098 MPa. The measured maximum reflected pressure, 2.380 MPa, is 13.44% higher than the mean value. The measure maximum reflected pressure is 23.44% higher than the mean value of reflected impulse.

Table 5: Recorded reflected pressure data for test shot 5

	td (ms)	Pr (Mpa)	Ir (Mpa.ms)
Point 1	5.7	1.947	2.541
Point 3	8.9	2.054	3.881
Point 4	10	2.012	3.24
Point 5	5.2	2.38	2.915
Mean Value	7.5	2.098	3.144

Empirical equations as provided in the previous chapter of the work are often used to determine the loading properties of the blast charges. In order to compare the result of experimental blast wave characteristics with the predicted loading, empirical or semi empirical equations that had been proposed by number of researchers were used. The blast load parameters that were obtained by empirical formulas were observed to give relatively lower loading parameters compared to the measured data.

The predicted peak overpressure values from these equations are presented in Table 6. Brode (1977) suggested using Equation (1.7) to calculate peak overpressure that is

higher than 10 bar. For the peak overpressure that is between 0.1 and 10 bars, Brode (1977) proposed another Equation (1.8). The peak overpressure that is predicted by the study of Kinney and Graham (1985) (Eq.1.21) is also presented in Table 6.

Table 6: Calculated peak overpressure

Ps	Peak Overpressure calculations:	
Brode 1955		
2.379 bar	237.86 kPa	Ps>10 bar
2.267 bar	226.742 kPa	0.1<Ps<10 bar
Kinney&Graham 1985		
3.023242 bar	302.324 kPa	

By using the peak overpressure value, Brode suggested that reflected pressure can be calculated (1977). The related equation can be observed in Equations (1.18) and (1.19). (Rankine and Hugoniot equations is similar to this equation as Brode equations are based on their studies with the assumption that that air is an ideal gas with a constant gamma of 1.4). It can be seen from Table 7 that the calculated reflected pressure based on empirical formulae is 1115.3 kPa. It is 30.6% lesser than the mean value of the experimental results. Moreover, it is 17.15% lower than the minimum reflected pressure obtained from experiment. The impulse values were obtained from the empirical equations are presented in Table 8. As can be seen from this table, the integrated modified Friedlander Equation (1.2) yielded the same result with the equation suggested by Kinney and Graham (1985). The time varying overpressure, $P(t)$, calculated according to modified Friedlander equation that is suggested by Baker, 1973 (Equation 1.2) is presented in Figure 16. It should be noted that is not the reflected pressure but the pressure of the blast wave.

Table 7: Calculated reflected pressure

Pr	Reflected Pressure calculations:	
Brode 1977		
11.51776 bar	1151.776 kPa	Ps<6.9 bar
11.15299 bar	1115.299 kPa	Ps>6.9 bar
Rankine&Hugoniot		
11.51776 bar	1151.776 kPa	

Table 8: Calculated reflected impulse

Ir	Reflected Pressure Impulse calculations:
Kinney&Graham 1985	
11.9925	1199.25 kPa.ms
Integral P(t)	
11.9925	1199.25 kPa.ms

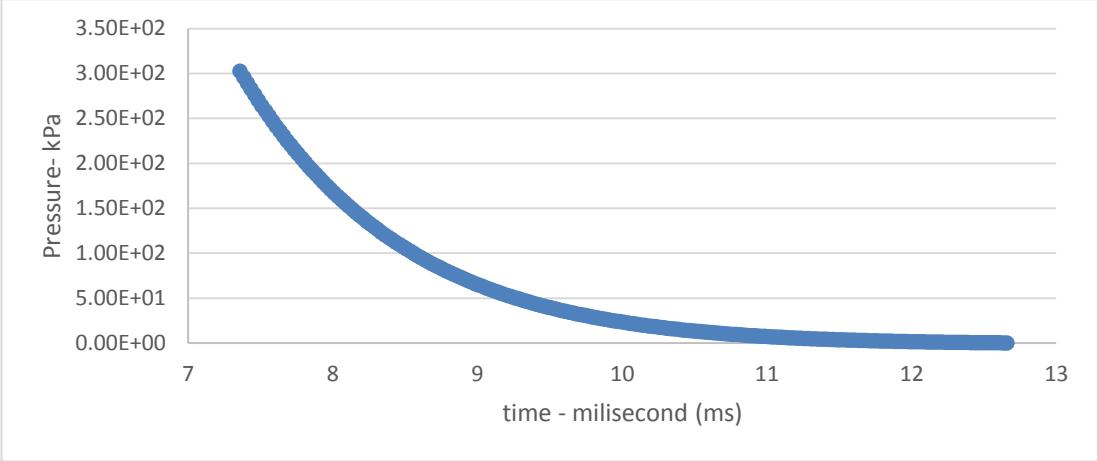

Figure 16: Modified Friedlander Equation- Peak overpressure time history

In summary, these calculations show that the predicted/calculated blast wave parameters are lower than the results obtained by experiment. Consequently, the results of the experiment that had been conducted by Nassr were used as the loading properties for this study.

The data of Point 3 which has recorded a higher impulse value was chosen as the loading condition to calibrate the Johnson-Cook constitutive model parameters in the finite element models. The blast loading and axial load properties can be seen in Tables 9 and 10 for shots 3 and 5, respectively.

Table 9: Blast load parameters for shot 3 – 3C1

Charge Weight	Stand-off Distance	Scaled Distance	ta	td	Pr	Ir	Axial Load
ANFO (kg)	m	Z	ms	ms	Mpa	Mpa.ms	kN
150	9.0	1.69	5	6.1	1.484	2.688	270

Table 10: Blast load parameters for shot 5 – 5C1

Charge Weight	Stand-off Distance	Scaled Distance	ta	td	Pr	Ir	Axial Load
ANFO (kg)	m	Z	ms	ms	Mpa	Mpa.ms	kN
250	9.5	1.51	5	8.9	2.054	3.881	640

The reflected pressure-time histories for both shot 3 and 5 were constituted by using the Modified Friedlander equation with β decay coefficient and the recorded data for each shot that were obtained from the experiment conducted by Nassr et al. (2012). In order to construct the time pressure histories, it is required to determine β coefficient. The β coefficients were determined as -3.516 and -1.989 for shots 3 and 5, respectively. The reflected pressure-time histories for the shots 3 and 5 are provided in Figure 17.

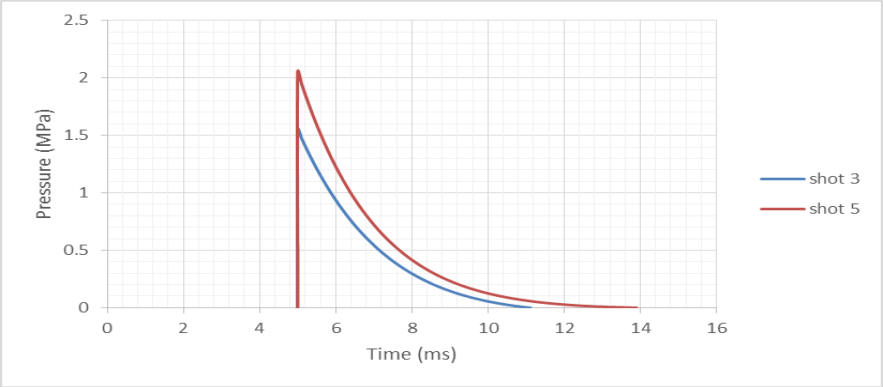

Figure 17: Reflected pressure-time histories of Shot 3 and Shot 5

The calculated natural period of the element was about 0.009 seconds: in order to obtain the static axial load, the beam-column element was loaded axially by a ramp function over a period of 0.05 seconds. The axial load was then kept constant throughout the blast step after 0.05 seconds and blast loading was analyzed afterwards with a duration of 0.03 seconds. The models were analyzed on a PC with a processor i7-2670QM CPU at 2.20 GHz and 6.00 GB RAM running on Windows 7. In the analysis steps, automatic time increments were used utilizing the element by element stable increment estimator of the code. The calculated stable time increment was about 1.47 x 10-7 sec. The solution time for static axial loading was about 60 minutes and 36 minutes of solution time was required to analyze the blast loading step. The large deformation effect was taken into account by activating the "Nlgeom" command in ABAQUS.

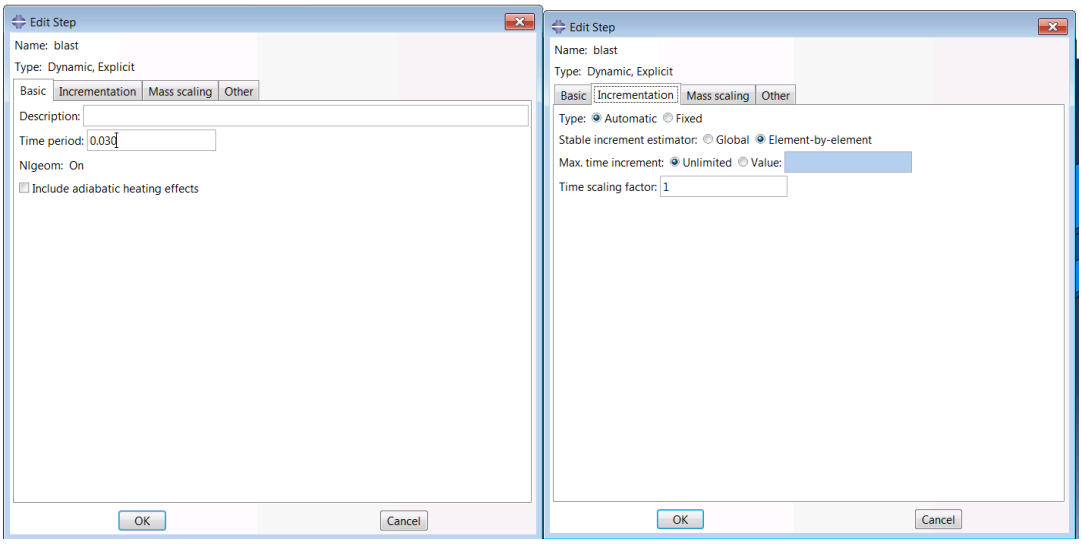

Figure 18: User Interface of ABAQUS CAE

2.2.3 Material Modelling

The density, Young's Modulus and the Poisson's ratio of steel were taken as 7850 kg/m^3, 205 GPa and 0.29, respectively. Johnson-Cook plasticity with Johnson-Cook rate dependent hardening was used to simulate the nonlinear behavior of the steel elements. As can be seen from Table 3 given in Section 2.1.2, the yield strength and ultimate strength of the section W150x24 are 393 MPa and 537 MPa, respectively. With the purpose of choosing the advanced modeling parameters of the model reflecting the actual steel elements' strength characteristics, a review of the literature was conducted for the Johnson-Cook model. There is a lack of information in the open literature about the Johnson-Cook Constitutive model parameters for different steel types subjected to blast loading. Consequently, the calibration process was initialized using the AISI 1045 steel Johnson-Cook parameters for shot 3. As can be observed from Table 11, AISI 1045 steel strength characteristics are well-matched with the W150x24 section.

Table 11:AISI 1045 steel strength characteristics

Section Size	***Yield Stress Mpa***	***Ultimate Strength Mpa***
AISI 1045	310	565

Özel and Karpat (2007) studied the optimized Johnson-Cook constitutive model parameters for different steel types and stress ranges for high strain rate metal cutting conditions using evolutionary computational algorithms. The tabulated form of the starting and resulting values of the optimization process that was conducted by Özel and Karpat can be observed in Table 12.

Table 12: Johnson- Cook Plasticity Parameters for AISI 1045 (Özel and Karpat, 2007)

	A	B	n	C	$\dot{\varepsilon}_0$
Starting Values	553.1	600.8	0.234	0.0134	7500
Resulting Values	731.63	518.7	0.3241	0.00571	7500

The resulting values of the optimization process that had been conducted by Özel and Karpat were used as starting point to calibrate the J-C constitutive model parameters of the section W150x24. As there are no studies to identify the J-C constitutive model parameters for section size W200x71 in open literature, DH-36 steel that has similar strength characteristics was used as starting point. The strength characteristics of DH-36 steel are given in Table 13.

Table 13: DH-36 steel strength characteristics

Section Size	***Yield Stress Mpa***	***Ultimate Strength Mpa***
DH-36	355	490

Gambirasio and Rizzi (2014) compared different strategies that can be adopted to calibrate Johnson-Cook constitutive model parameters for different type of steel sections. The J-C constitutive model parameters calibrated for DH-36 are given in the Table 14. The results of this study were used to calibrate the constitutive model parameters for section W200x71.

Table 14: Johnson- Cook Plasticity Parameters for DH 36 (Gambirasio and Rizzi, 2014)

A	B	n	C	$\dot{\varepsilon}_0$
915.56	760.78	0.601	0.0156	0.001

The temperature softening in Johnson-Cook constitutive model was not used in this study. The temperature change caused by free air-burst explosion is usually ignored by researchers because of the very short duration of shock wave influence and the distance between the point of interest and explosion center. Excluding the studies that were conducted to investigate the effect of fire caused by explosion, the effect of the temperature change is generally not included in material modelling in most of the FEM analysis (Liew, 2007, Cabello, 2011). In addition to these, the data about

temperature change caused by explosion were not included in the documentation of the testing by Nassr et al. (2012).

2.3 Calibration of the Johnson-Cook Constitutive Model Parameters

Accurate modelling of dynamic mechanical behavior is a prerequisite for an effective analysis for blast loading. In order to represent the plasticity behavior of steel members exposed to blast loading, reliable rate-dependent constitutive models are required. The success of a particular constitutive model depends on how effectively it represents the mechanics of blast loading as well as its ability to capture all relevant deformation parameters in a constitutive equation. In this study, one of the objectives is to recalculate the parameters of the constitutive model determined by other researchers for simulating the response for different dynamic conditions. In order to achieve this goal, the experimental data obtained by Nassr (2012) were used as a convergence points for calibration processes with two different starting points that have been obtained by other researchers.

As mentioned before, the research of Özel and Karpat (2007) was used as starting point to calibrate the section W150x24. The calibrated constitutive model parameters and the deviation from the experimental data expressed in terms of the errors in the maximum displacement and strain values can be seen in Table 15. The maximum displacement that is observed at the mid-span of back flange was 29.4 mm for section W150x24. The strain time history for the calibrated model is compared to the experiment in Figure 19. The displacement time histories of the experiment and calibrated model are compared in Figure 20 for the point 3 data. Calibrated models simulate the experiment well as shown in both figures.

Table 15: Calibrated Constitutive Model Parameters for section W150x24

	Constitutive Model Parameters					Maximum Displacement	Maximum Strain	Calculated	Calculated
	A	B	n	C	$\dot{\varepsilon}_0$	y-axis (mm)	y-axis (με)	Error %	Error %
Experiment Results						30.900	1500		
Calibrated Model	575.00	975.00	0.120	0.00571	7500	29.399	1118.89	4.86%	25.41%

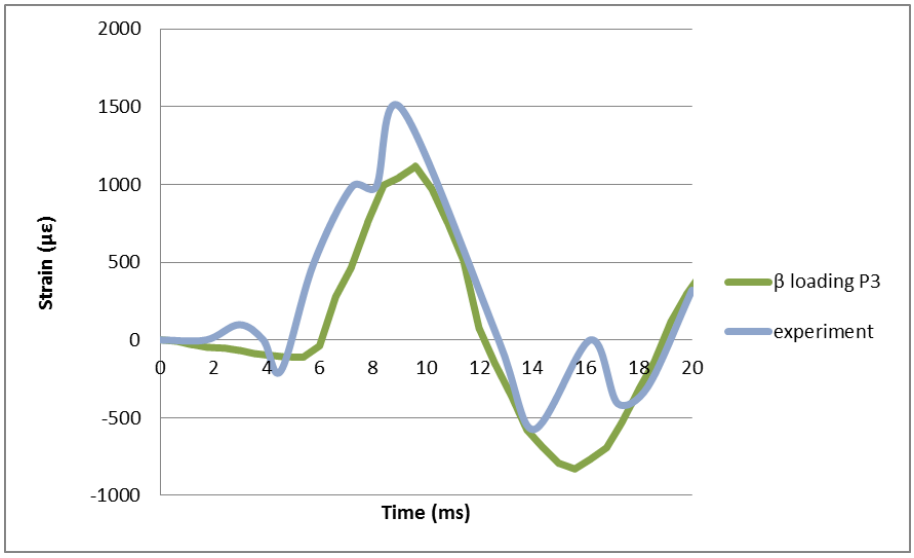

Figure 19: Strain-time history of the experiment and the calibrated model, shot 3

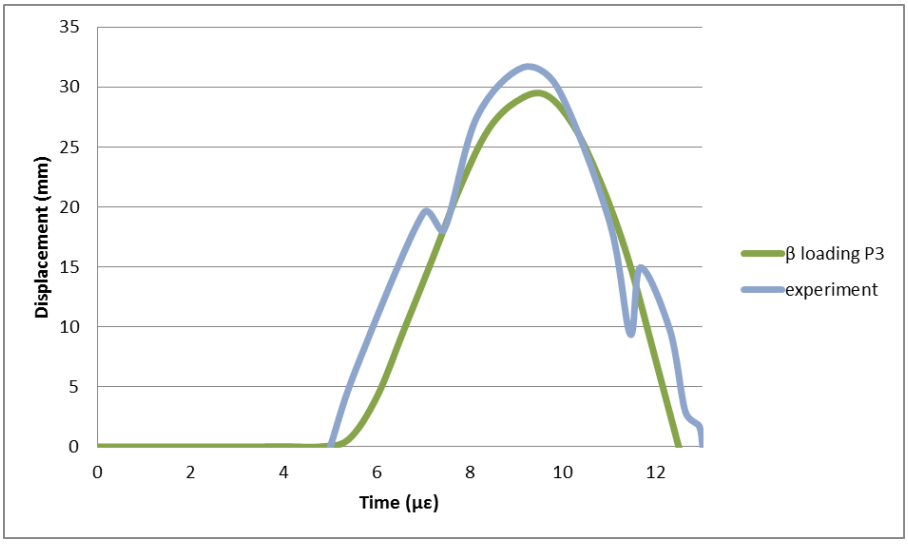

Figure 20: Displacement-Time History of experiment and calibrated model shot 3

The contour values of the maximum displacement and strain values predicted on the whole specimen are presented in Figures 21 and 22, respectively. The observed maximum strain of section W150x24 at the mid-span of the back flange was 1119 με.

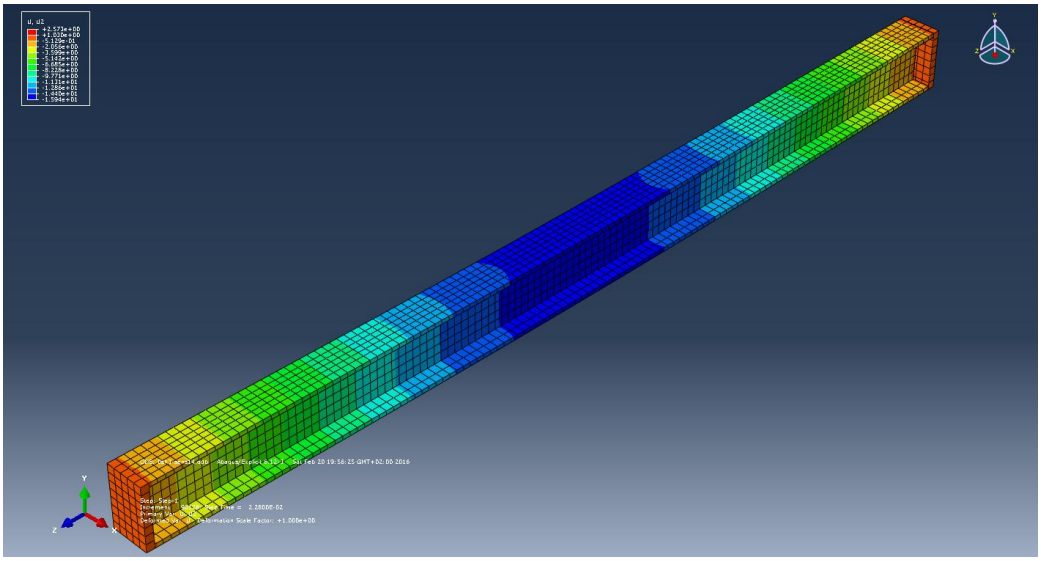

Figure 21: Maximum diplacement of section W150x24 in U2 direction

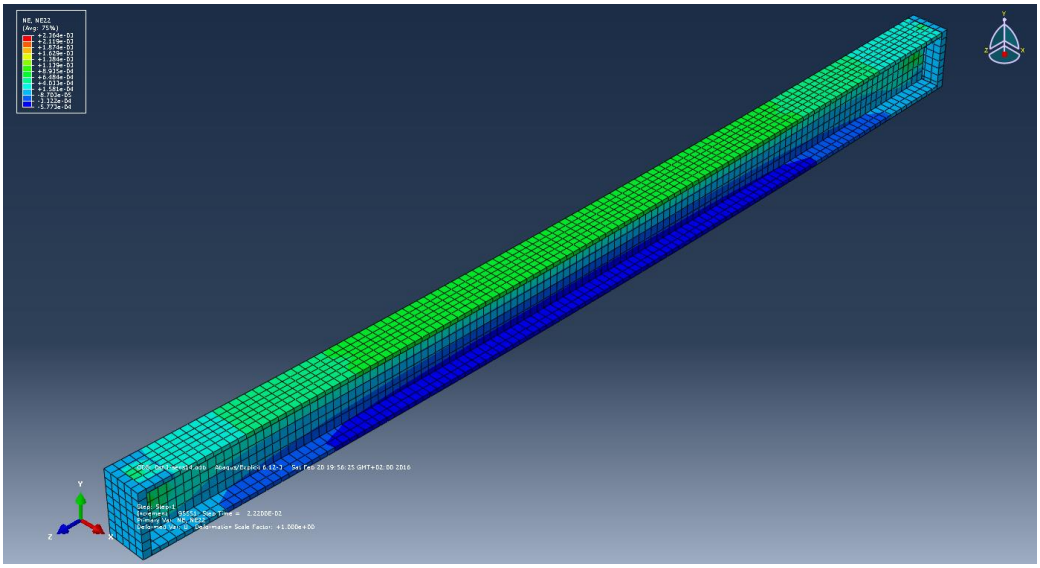

Figure 22: Maximum strain of section W150x24 in N2 direction

As mentioned before, the DH-36 steel properties given by Gambirasio and Rizzi (2014) were used as the starting point for the calibration of the J-C constitutive model parameters for section W200x71. The final J-C model parameters are presented in Table 16.

Table 16: Calibrated Constitutive Model Parameters for section W200x71

	Constitutive Model Parameters				
	A	B	n	C	$\dot{\varepsilon}_0$
Experiment Results					
Calibrated model	350.00	550.00	0.2758	0.0132	0.1

The permanent deflection, maximum displacement and the maximum strain values of both experiment and calibrated model of section W200x71 are provided in Table 17. The deviation from the experimental data expressed in terms of the errors in the maximum displacement and strain values can be seen in the same table.

Table 17: Results of calibrated model of section W200x71

	Permenant Deflection (mm)	Maximum Displacement y-axis (mm)	Maximum Strain y-axis (με)	Error in Permenant Deflection %	Error in Maximum Displacement	Error in Maximum Strain %
Experiment Results	32.8	71	3960			
Calibrated model	37.70	61.25	3367	14.95%	13.73%	14.96%

The strain time histories of the experiment and the calibrated model are compared in Figure 23. The peak time history timing was almost identical. The time histories compare favorably with the general shapes are similar.

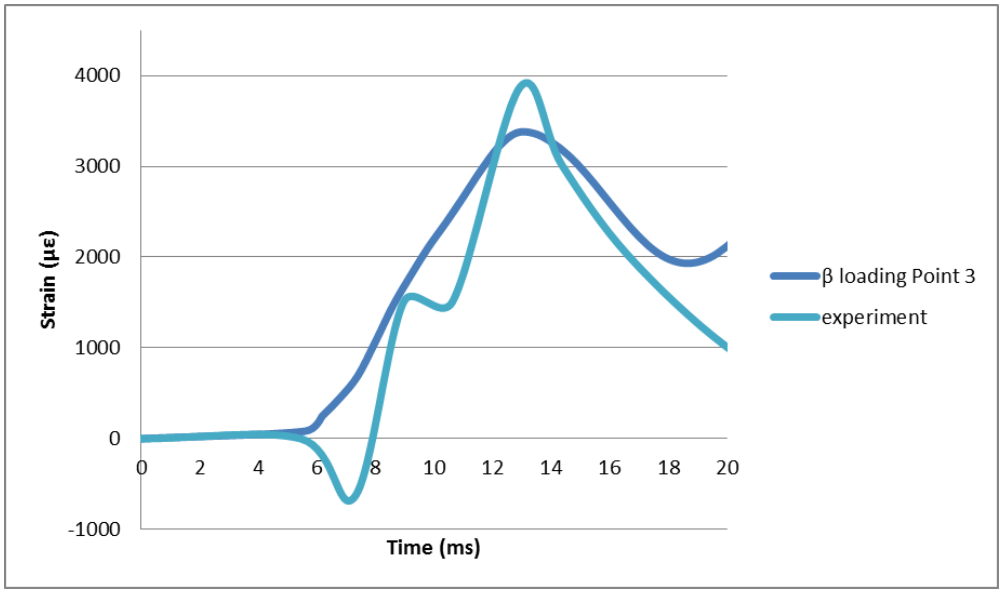

Figure 23: Strain-Time History of experiment and calibrated model shot 5

The displacement time histories of the experiment and the calibrated model of section W200x71 (Figure 24) show that there is time lag in the peak response between the experiment and the model. The displacement data of section W200x71 (5C1) was not recorded (Nassr et.al. 2012) because of the destruction of the displacement transducer at that point: consequently, the displacement time history of column was calculated by integrating the strain time history. There is a time lag between the peak displacement values of the experiment and the calibrated model. The time difference between peak values is 5 ms.

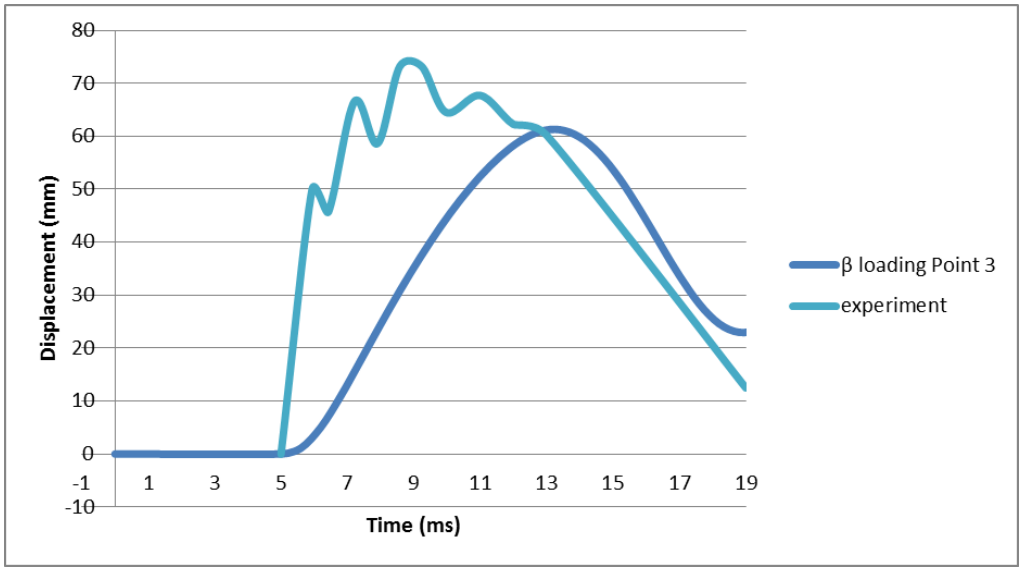

Figure 24: Displacement-Time History of experiment and calibrated model shot 5

The maximum displacement and strain contours for the W200x71 section are presented in Figures 25 and 26, respectively.

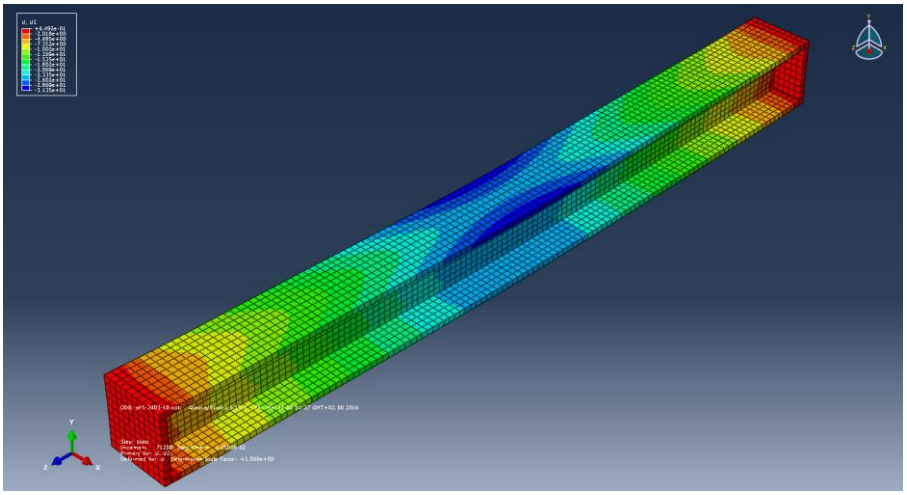

Figure 25: Maximum diplacement of section W200x71 in U2 direction

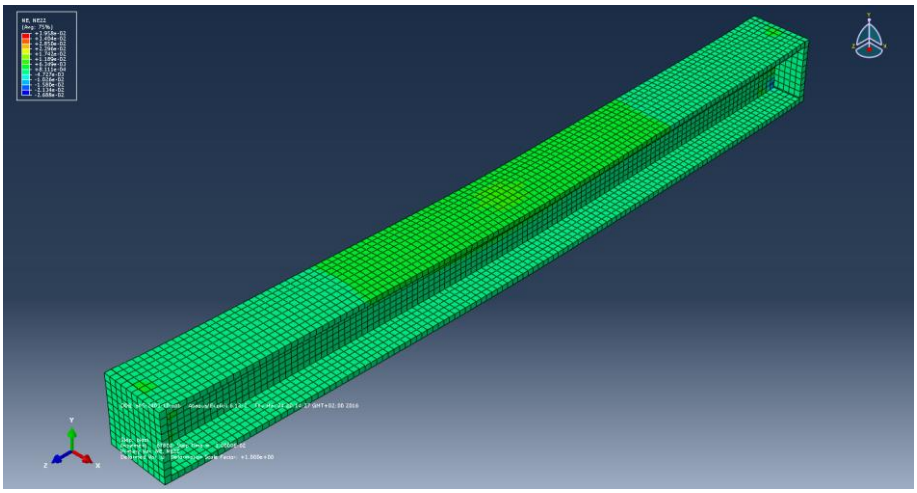

Figure 26: Maximum strain of section W200x71 in N2 direction

CHAPTER 3

SENSITIVITY ANALYSIS FOR JOHNSON-COOK MODEL PARAMETERS

3.1 Parametric Study

In order to examine the effect of modeling variables on the dynamic response of the steel beam-column element, a parametric study was conducted. The Johnson – Cook constitutive model parameters were treated as random variables and the tornado diagrams were prepared to show the influence of different parameters on the simulation results. The control model is the calibrated model in this study. In the following section, the effects of the J-C parameters that had been varied in the same range were presented. The presented results were obtained by reducing and increasing the related parameter by 16.67 % and 12.50 %, respectively. In the calibration process it was observed that changes like 25%, 45% on each parameter value resulted in too much difference in the analysis results. For instance, although section size W150x24 namely 'shot 3' behaves in elastic manner (Nassr, 2012), the reduction of the parameter 'A' by 35% in the model yielded plastic deformation in the simulation. In order to investigate the effects of the variance of the parameters on the response of the structural element in a plausible range, the changes in parameters were kept small.

The results of the sensitivity study that was conducted for the W150x24 section can be seen in Table 18. The maximum displacement and maximum strain values showed that the increase and decrease in related parameters resulted in very small variations in the results. This is expected given the linear nature of the experiment and the chosen parameters representing this behavior without too much alteration with the Johnson-Cook Constitutive model remaining in the linear range.

Table 18: Results of Parametric Study for Shot 3

	Constitutive Model Parameters					Maximum	Maximum	Calculated	Calculated
	A	B	n	C	$\dot{\varepsilon}_0$	Displacement y-axis	Strain y-axis	Error %	Error %
Experiment Results						30.900	1500		
Calibrated Model	575.00	975.00	0.120	0.00571	7500	29.399	1118.89	4.86%	25.41%
-16.67% A	479.15	975.00	0.120	0.00571	7500	29.426	1133.05	4.77%	24.46%
-12.50% A	503.13	975.00	0.120	0.00571	7500	29.414	1127.71	4.81%	24.82%
+12.50% A	646.88	975.00	0.120	0.00571	7500	29.397	1117.98	4.86%	25.47%
+16.67% A	670.85	975.00	0.120	0.00571	7500	29.397	1118.06	4.86%	25.46%
-16.67% B	575.00	812.47	0.120	0.00571	7500	29.407	1122.25	4.83%	25.18%
-12.50% B	575.00	853.13	0.120	0.00571	7500	29.404	1121.07	4.84%	25.26%
+12.50% B	575.00	1096.88	0.120	0.00571	7500	29.398	1118.36	4.86%	25.44%
+16.67% B	575.00	1137.53	0.120	0.00571	7500	29.398	1118.38	4.86%	25.44%
-16.67% n	575.00	975.00	0.100	0.00571	7500	29.397	1117.82	4.86%	25.48%
-12.50% n	575.00	975.00	0.105	0.00571	7500	29.398	1118.03	4.86%	25.46%
+12.50% n	575.00	975.00	0.135	0.00571	7500	29.405	1122.20	4.84%	25.19%
+16.67% n	575.00	975.00	0.140	0.00571	7500	29.408	1124.06	4.83%	25.06%
-16.67% C	575.00	975.00	0.120	0.00476	7500	29.399	1118.89	4.86%	25.41%
-12.50% C	575.00	975.00	0.120	0.00500	7500	29.399	1118.89	4.86%	25.41%
+12.50% C	575.00	975.00	0.120	0.00642	7500	29.399	1118.89	4.86%	25.41%
+16.67% C	575.00	975.00	0.120	0.00666	7500	29.399	1118.89	4.86%	25.41%
$\dot{\varepsilon}_0$ =0.1	575.00	975.00	0.120	0.00571	0.1	29.400	1119.05	4.86%	25.40%
$\dot{\varepsilon}_0$ =1	575.00	975.00	0.120	0.00571	1	29.400	1119.06	4.86%	25.40%
$\dot{\varepsilon}_0$ =10	575.00	975.00	0.120	0.00571	10	29.399	1118.89	4.86%	25.41%
$\dot{\varepsilon}_0$ =100	575.00	975.00	0.120	0.00571	100	29.399	1118.89	4.86%	25.41%

On the other hand, the section W200x71 namely ‘shot 5’ did experience plastic deformations and the results of sensitivity analysis conducted by changing plasticity parameters are given in the following sections.

3.1.1 Effect of Parameter ‘A’

A parametric study was conducted to examine the effect of J-C constitutive model parameter ‘A’ on the permanent deflection, maximum displacement and the maximum strain of ‘shot5’. The following table provides the constitutive model parameters that were used in the model and the analysis results which are permanent deflection, maximum displacement and maximum strain values at the ½ length of the beam. This table shows that as the Parameter ‘A’ increases strain and displacement values decreases.

Table 19: Effect of Parameter 'A'

	Constitutive Model Parameters					Permanent Deflection (mm)	Maximum Displacement y-axis (mm)	Maximum Strain y-axis (με)
	A	B	n	C				
Experiment Results						32.8	71	3960
Calibrated model	350.00	550.00	0.2758	0.0132	0.1	37.70	61.25	3367
-16.67% A	291.66	550.00	0.2758	0.0132	0.1	55.82	77.96	4629
-12.50% A	306.25	550.00	0.2758	0.0132	0.1	50.59	73.21	4242
+12.50% A	393.75	550.00	0.2758	0.0132	0.1	28.23	52.63	2513
+16.67% A	408.35	550.00	0.2758	0.0132	0.1	25.70	50.47	2316

The rate of change in the model predictions that were obtained by changing value of parameter ‘A’ is presented in Table 20. The percentage values were calculated according to the calibrated model results. For instance, as the parameter ‘A’ decreased by 16.67%, permanent deflection value is 48.04% higher than the calibrated model. The associated displacement-time histories of the models which have different parameter ‘A’ values are presented in Figure 27.

Table 20: Rate of Change in Analysis Results-Parameter ‘A’

	Rate of Change in Permanent Deflection %	Rate of Change in Maximum Displacement %	Rate of Change in Maximum Strain %
-16.67% A	48.04%	27.28%	37.46%
-12.50% A	34.18%	19.52%	25.97%
+12.50% A	25.12%	14.08%	25.37%
+16.67% A	31.83%	17.60%	31.22%

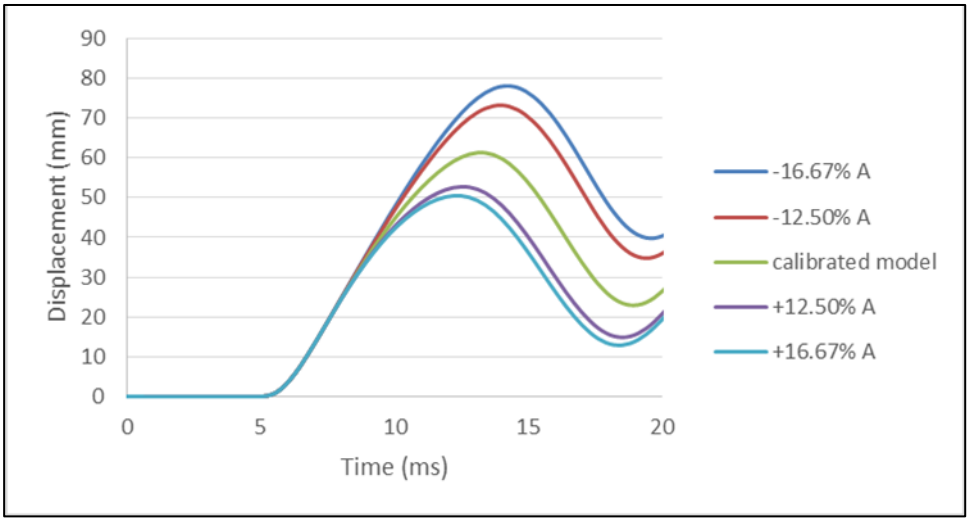

Figure 27: Parameter 'A' - Displacement Time History

The strain-time histories for the sensitivity analysis of Parameter ‘A’ are presented in Figure 28. When the time-history diagrams are examined, it is seen that as the parameter ’A’ decreases, the history diagrams shift upward and the amount of shift increases slightly.

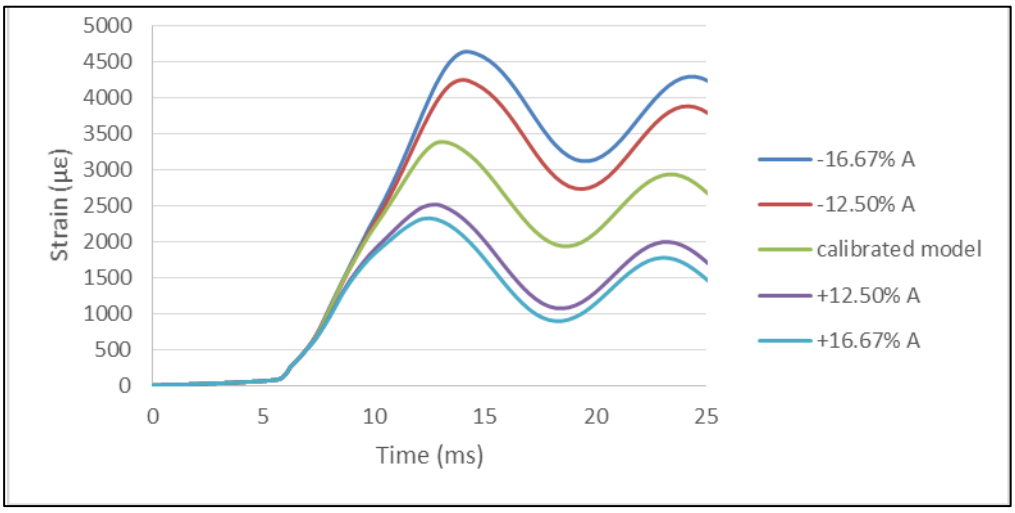

Figure 28: Parameter 'A' - Strain Time History

The following tornado diagrams (Figure 29, 30 and 31) show the effect of Parameter ‘A’ on the permanent deflection, maximum displacement and the maximum strain results. The red bar represents effect of increase in the parameter and the blue bar gives the effect of parameter when it decreases.

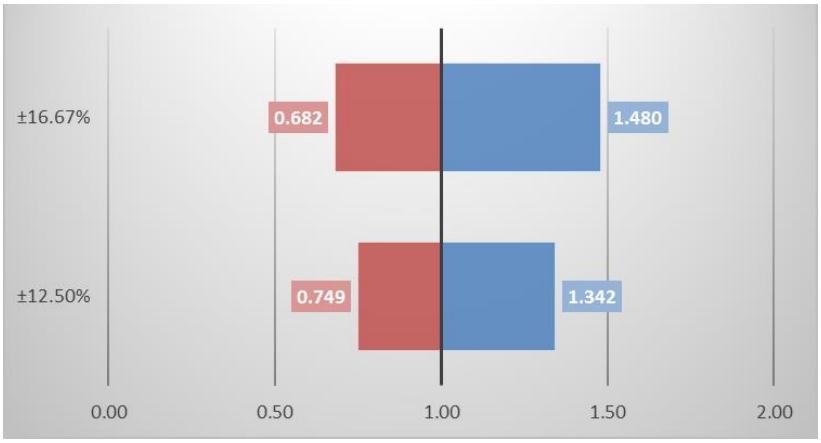

Figure 29: Effect of parameter 'A' on permanent deflection

The model which has the parameter ‘A’ value increased by 16.67%, yields a permanent deflection of 0.682 times the calibrated model result. Additionally, as the parameter ‘A’ decreased by 12.50%, the model yields a permanent deflection value as 1.342 times the result of calibrated model.

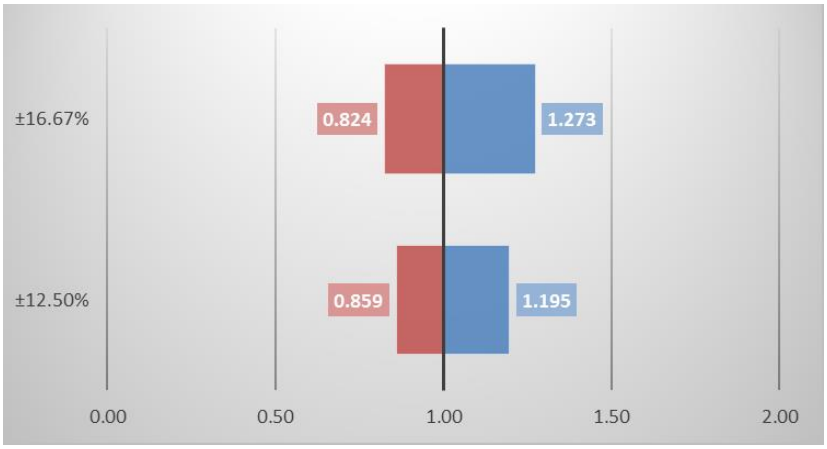

Figure 30: Effect of parameter 'A' on maximum displacement

The effect of parameter ‘A’ is lesser on maximum displacement than the permanent deflection.

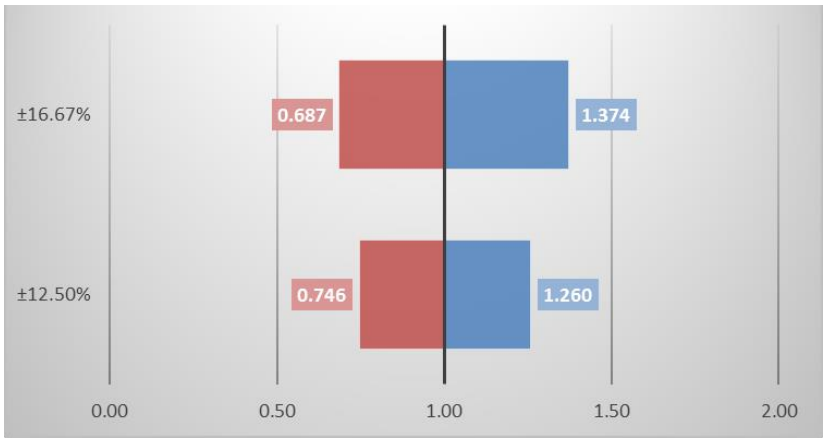

Figure 31: Effect of parameter 'A' on maximum strain

As it is expected, the change in parameter ‘A’ has a very similar effect on the maximum strain and permanent deflection. Moreover, it can be seen from the tornado diagrams, the change in parameter ‘A’ has more influence on the maximum strain and permanent deflection values.

3.1.2 Effect of Parameter ‘B’

Another parametric study was conducted to investigate the effect of J-C constitutive model parameter ‘B’ on the results of the finite element model. In the following table, the associated model parameters and the corresponding results can be observed for each model.

Table 21: Effect of parameter 'B'

	Constitutive Model Parameters					Permenant Deflection (mm)	Maximum Displacement y-axis (mm)	Maximum Strain y-axis (με)
	A	B	n	C				
Experiment Results						32.8	71	3960
Calibrated model	350.00	550.00	0.2758	0.0132	0.1	37.70	61.25	3367
-16.67% B	350.00	458.32	0.2758	0.0132	0.1	47.26	69.61	3841
-12.50% B	350.00	481.25	0.2758	0.0132	0.1	44.57	67.14	3678
+12.50% B	350.00	618.75	0.2758	0.0132	0.1	32.25	56.59	2886
+16.67% B	350.00	641.69	0.2758	0.0132	0.1	30.65	55.22	2742

The decrease of parameter 'B' is similar to the decrease of parameter 'A' in such a way that they both cause an increase in displacement and strain values. The rate of change percentages calculated according to the calibrated model results are presented in Table 22. The increase in the parameter 'B' resulted in almost the same rate of change in the maximum strain and permanent deflection. However, when the parameter 'B' is decreased, the rate of change in the permanent deflection was larger than the rate of change of maximum strain. The displacement-time and strain-time histories of the models with different 'B' values are presented in the Appendix A.

Table 22: Rate of Change in Analysis Results-Parameter 'B'

	Rate of Change in Permanent Deflection %	Rate of Change in Maximum Displacement %	Rate of Change in Maximum Strain %
-16.67% B	25.34%	13.65%	14.06%
-12.50% B	18.22%	9.61%	9.22%
+12.50% B	14.47%	7.61%	14.30%
+16.67% B	18.70%	9.84%	18.57%

The tornado diagrams that were obtained using variations in the B parameter are presented as follows. Figures 32, 33 and 34 show the variations in the maximum displacement, strain and the permanent deformation, respectively. It can be seen from the Figures 33 and 34 that the change in parameter 'B' has a similar effect on the permanent deflection and maximum strain values and has less influence on the maximum displacement.

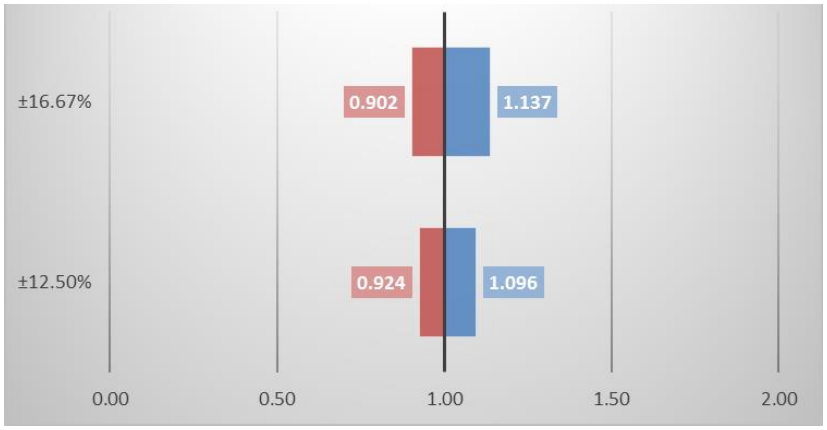

Figure 32: Effect of parameter 'B' on maximum displacement

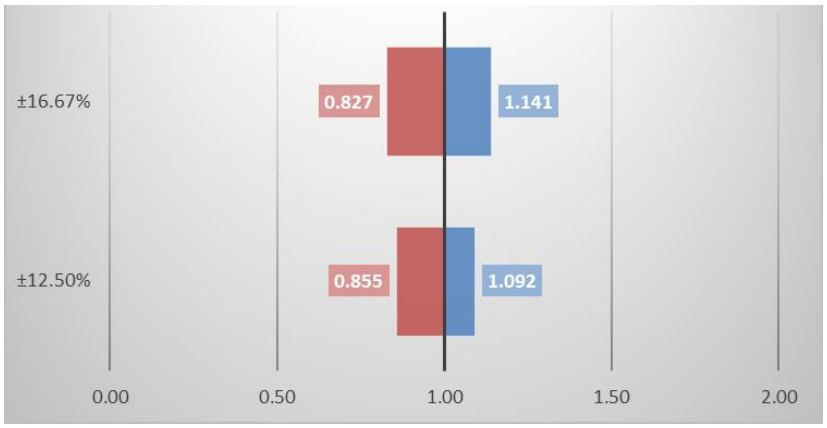

Figure 33: Effect of parameter 'B' on maximum strain

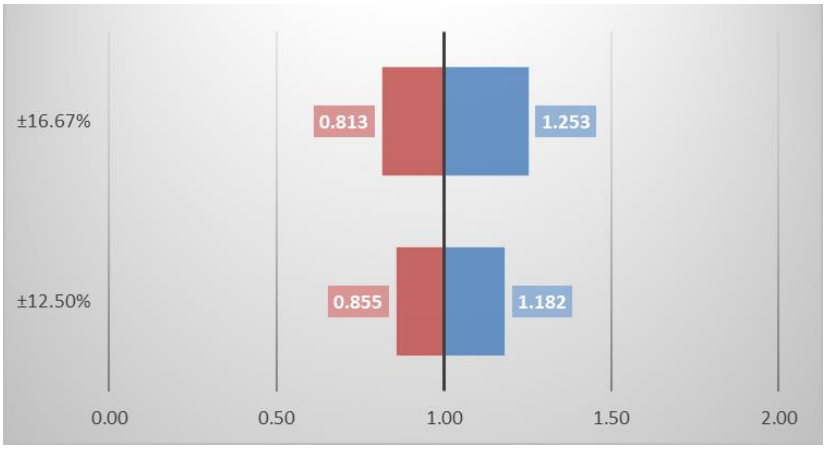

Figure 34: Effect of parameter 'B' on permanent deflection

3.1.3 Effect of Parameter ‘n’

The results of the parametric studies that was conducted to study the effect of J-C constitutive model parameter ‘n’ on the maximum displacement and strain are presented in Table 23.

Table 23: Effect of parameter 'n'

	Constitutive Model Parameters					Permenant Deflection (mm)	Maximum Displacement y-axis (mm)	Maximum Strain y-axis (με)
	A	B	n	C				
Experiment Results						32.8	71	3960
Calibrated model	350.00	550.00	0.2758	0.0132	0.1	37.70	61.25	3367
-16.67% n	350.00	550.00	0.2298	0.0132	0.1	25.90	50.79	2245
-12.50% n	350.00	550.00	0.2413	0.0132	0.1	28.63	53.12	2484
+12.50% n	350.00	550.00	0.3103	0.0132	0.1	47.68	70.28	3987
+16.67% n	350.00	550.00	0.3218	0.0132	0.1	51.16	73.52	4313

The decrease in the value of parameter ‘n’ results in an increase in the maximum displacement and the maximum strain. Unlike the parameters ‘A’ and ‘B’, the decrease in the parameter ‘n’ caused a reduction in the predicted results. The rate of change percentages calculated according to calibrated model results are presented in Table 24. The displacement-time and strain-time histories of the models which have different parameter ‘n’ were presented in Appendix A.

Table 24: Rate of Change in Analysis Results-Parameter ‘n’

	Rate of Change in Permanent Deflection %	Rate of Change in Maximum Displacement %	Rate of Change in Maximum Strain %
-16.67% n	31.30%	17.08%	33.33%
-12.50% n	24.05%	13.27%	26.23%
+12.50% n	26.48%	14.74%	18.40%
+16.67% n	35.70%	20.04%	28.08%

The tornado diagrams that were obtained using variations in the ‘n’ parameter are presented as follows. Figures 35, 36 and 37 show the variations in the maximum displacement, strain and the permanent deformation, respectively.

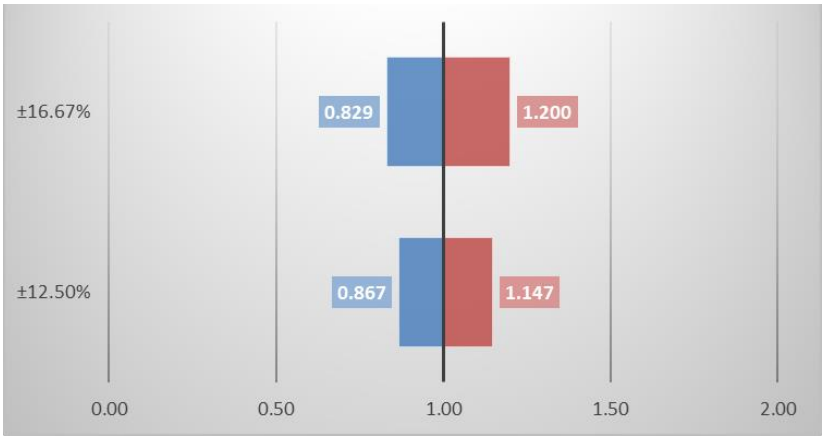

Figure 35: Effect of parameter 'n' on maximum displacement

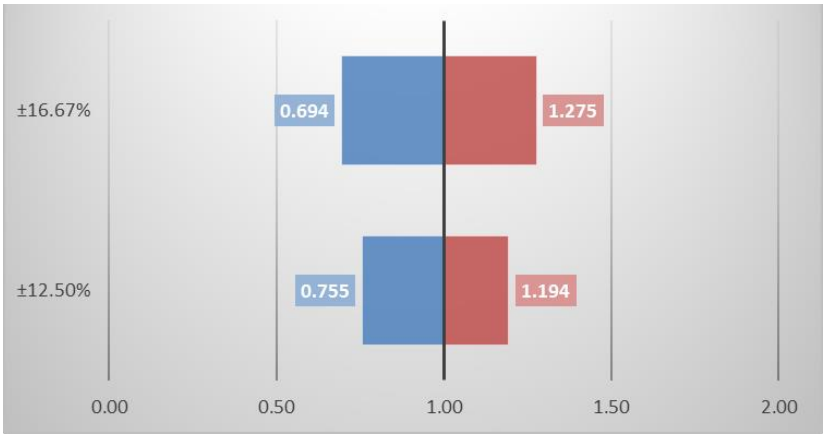

Figure 36: Effect of parameter 'n' on maximum strain

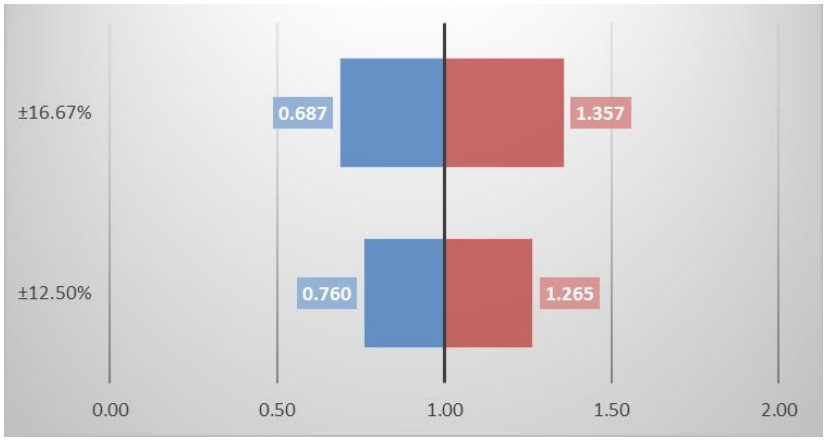

Figure 37: Effect of parameter 'n' on permanent deflection

3.1.4 Effect of Parameter ‘C’

The results of the finite element analysis according to different parameter ‘C’ values were provided in Table 25.

Table 25: Effect of parameter 'C'

	Constitutive Model Parameters					Permenant Deflection (mm)	Maximum Displacement y-axis (mm)	Maximum Strain y-axis (με)
	A	B	n	C				
Experiment Results						32.8	71	3960
Calibrated model	350.00	550.00	0.2758	0.0132	0.1	37.70	61.25	3367
-16.67% C	350.00	550.00	0.2758	0.0110	0.1	38.37	61.96	3304
-12.50% C	350.00	550.00	0.2758	0.0116	0.1	38.20	61.78	3289
+12.50% C	350.00	550.00	0.2758	0.0149	0.1	37.22	60.73	3204
+16.67% C	350.00	550.00	0.2758	0.0154	0.1	37.06	60.56	3192

The rate of change percentages calculated according to calibrated model results are presented in Table 26. The results of parametric study conducted to examine the influence of J-C constitutive model parameter ‘C’ on the permanent deflection, maximum displacement and the maximum strain showed that parameter ‘C’ has very little, almost no effect on the analyses results.

Table 26: Rate of Change in Analysis Results-Parameter 'C'

	Rate of Change in Permanent Deflection %	Rate of Change in Maximum Displacement %	Rate of Change in Maximum Strain %
-16.67% C	1.77%	1.15%	1.88%
-12.50% C	1.31%	0.86%	2.33%
+12.50% C	1.28%	0.85%	4.85%
+16.67% C	1.69%	1.13%	5.21%

The tornado diagrams that were obtained using variations in the 'C' parameter are presented in Figures 38, 39 and 40. By observing the tornado diagrams provided above, it can be said that parameter 'C' cause no significant change on the strain and displacement values.

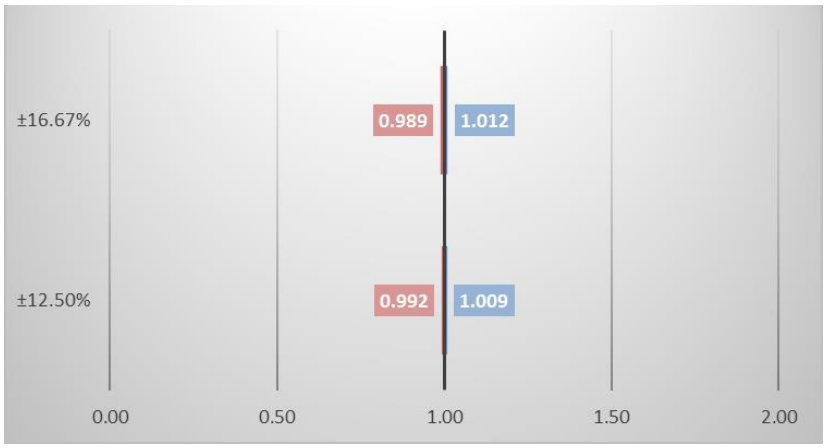

Figure 38: Effect of parameter 'C' on maximum displacement

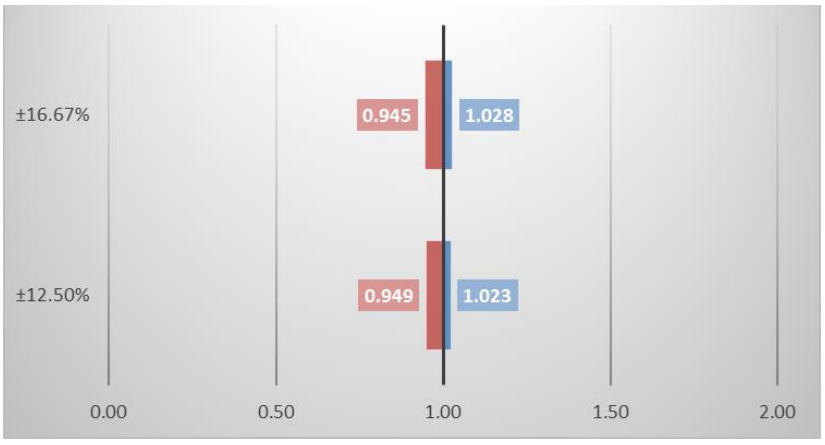

Figure 39: Effect of parameter 'C' on maximum strain

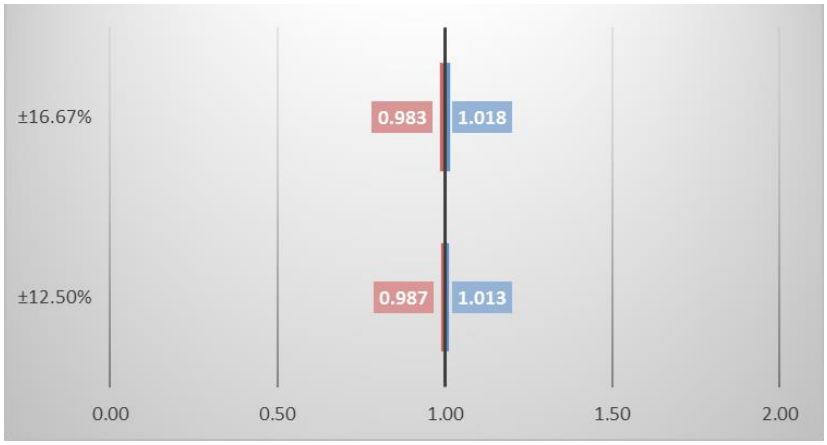

Figure 40: Effect of parameter 'C' on permanent deflection

3.1.5 Effect of Parameter '$\dot{\varepsilon}_0$'

Due to the fact that the parameter '$\dot{\varepsilon}_0$' is used in a logarithmic expression in the J-C constitutive model, the effect of parameter '$\dot{\varepsilon}_0$' was not studied in percentage. In order to observe the influence of parameter '$\dot{\varepsilon}_0$' four different values were studied. The models that have the parameter '$\dot{\varepsilon}_0$' equal to 1 or higher than 1 yields almost identical time history diagrams. The results of the sensitivity analysis of parameter '$\dot{\varepsilon}_0$' can be observed from the following table.

Table 27: Effect of parameter ' $\dot{\varepsilon}_0$'

	Constitutive Model Parameters					Permenant Deflection (mm)	Maximum Displacement y-axis (mm)	Maximum Strain y-axis (με)
	A	B	n	C				
Experiment Results						32.8	71	3960
Calibrated model	350.00	550.00	0.2758	0.0132	0.1	37.70	61.25	3367
$\dot{\varepsilon}_0$ =0.01	350.00	550.00	0.2758	0.0132	0.01	34.00	57.87	2936
$\dot{\varepsilon}_0$ =1	350.00	550.00	0.2758	0.0132	1	41.15	64.84	3612
$\dot{\varepsilon}_0$ =10	350.00	550.00	0.2758	0.0132	10	42.11	65.70	3619
$\dot{\varepsilon}_0$ =100	350.00	550.00	0.2758	0.0132	100	42.18	65.76	3632

The rate of change percentages calculated according to calibrated model results are presented in Table 28. As shown in the Tables 27 and 28, as the parameter '$\dot{\varepsilon}_0$' decreased, the experienced maximum strain was also decreased.

Table 28: Rate of Change in Analysis Results-Parameter '$\dot{\varepsilon}_0$'

	Rate of Change in Permanent Deflection %	Rate of Change in Maximum Displacement %	Rate of Change in Maximum Strain %
$\dot{\varepsilon}_0$ =0.01	9.81%	5.53%	12.81%
$\dot{\varepsilon}_0$ =1	9.14%	5.86%	7.27%
$\dot{\varepsilon}_0$ =10	11.68%	7.26%	7.47%
$\dot{\varepsilon}_0$ =100	11.88%	7.36%	7.85%

Although the strain rate that was captured in Nassr's experiment in shot 5 was 2.70 s^{-1}, in the calibrated model, the calculated maximum strain rate was obtained as 1.06 s^{-1}. In the research of Ngo et. al. (2007), it is stated that the blast phenomena typically resulted in high strain rates in the range of 10^2-10^4 s^{-1}. The strain rate values of both the experiment and FE model were lower than the values that were stated in the work of Ngo et. al. (2007).The effect of strain rate in the FE model is represented by the '$\dot{\boldsymbol{\varepsilon}}_{\mathbf{0}}$' quantity by the Johnson-Cook model. The effective stress vs. the effective plastic strain diagrams of a simple model with different '$\dot{\boldsymbol{\varepsilon}}_{\mathbf{0}}$' values can be seen from Figure 41. Although the ultimate strength values were not changing considerably, as the '$\dot{\boldsymbol{\varepsilon}}_{\mathbf{0}}$' value increased, the plastic strain capacity increased as well.

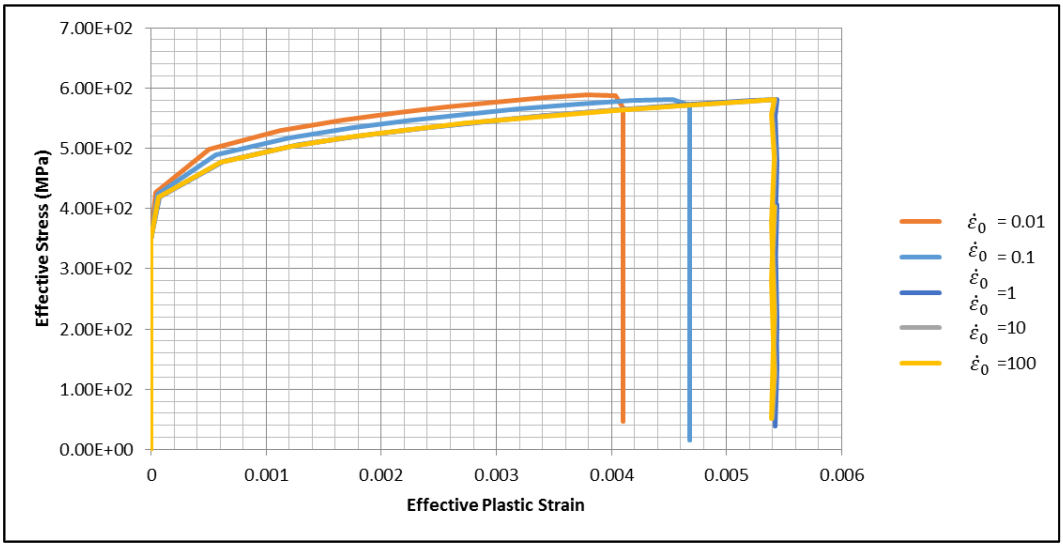

Figure 41: Effective Stress vs. Effective Plastic Strain

Parameter '$\dot{\varepsilon}_0$' was not examined in fixed percentage change as done with other parameters given the strain rate for the test. The figure above also shows the effect of the strain rate parameter on the modeling results to be minimal for the considered strain rate range. Consequently, the tornado diagrams were not prepared and the time history diagrams are given in Appendix A.

3.2 Tornado Diagrams

The first set of analyses examined the impact of reducing and increasing the J-C parameters in 16.67% on the results of the displacement and strain values. The same analyses were conducted by decreasing and increasing the J-C parameters by 12.50%. The results of the study can be observed in following figures (Figures 42-47). The red bar represents effect of increase in related parameter and the blue bar gives the effect of parameter when it decreases.

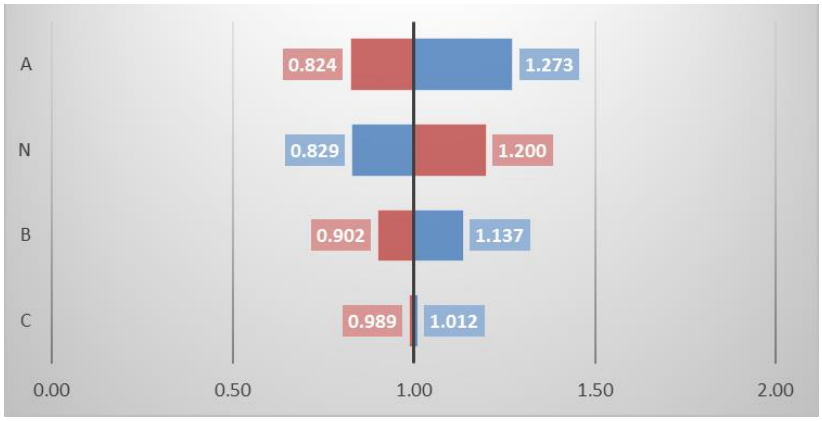

Figure 42: Tornado Diagram of Maximum Displacement ± 16.67%

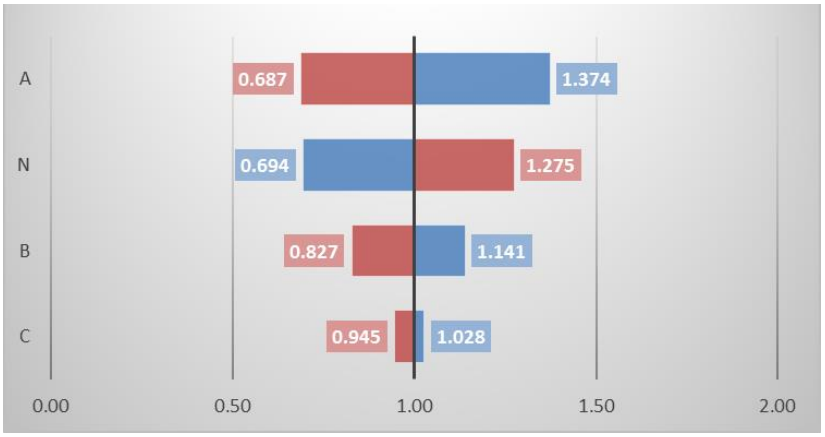

Figure 43: Tornado Diagram of Maximum Strain ± 16.67%

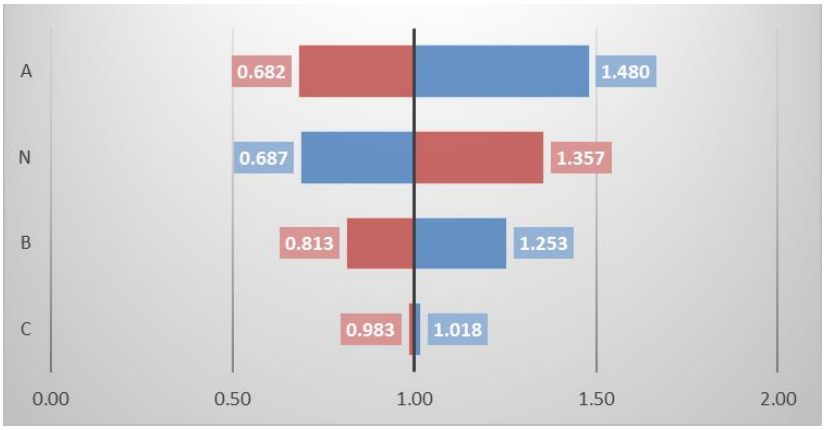

Figure 44: Tornado Diagram of Permanent Deflection ± 16.67%

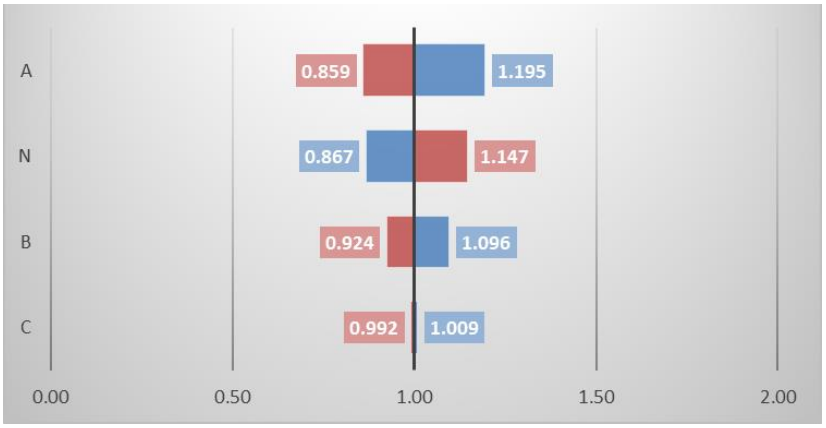

Figure 45: Tornado Diagram of Maximum Displacement ± 12.50%

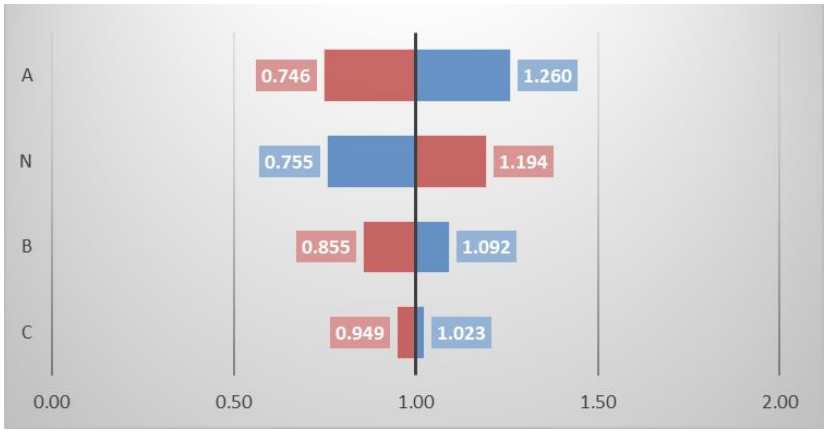

Figure 46: Tornado Diagram of Maximum Strain ± 12.50%

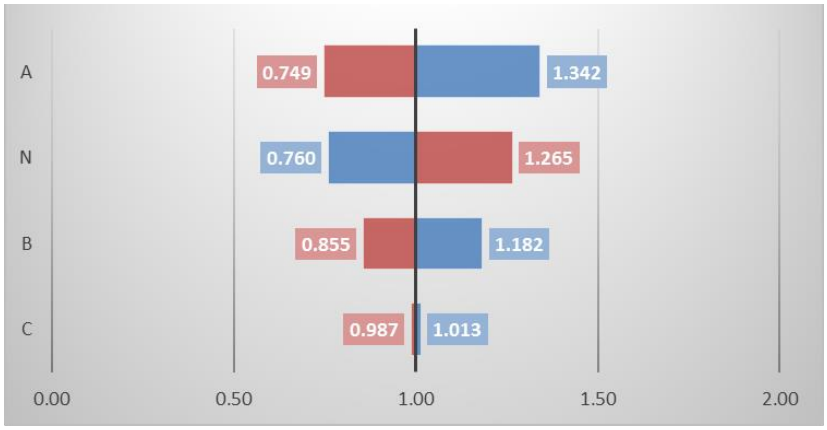

Figure 47: Tornado Diagram of Permanent Deflection ± 12.50%

The most effective parameter on the maximum strain and displacement results appears to be the parameter ‘A’, located on the top of the swing diagram with the longest bar. The next most effective parameter is the parameter ‘n’. The parameter ‘B’ follows the parameter ‘n’. The least important parameter is the parameter ‘C’, located at the bottom of the tornado diagram. The analysis results showed that the permanent deflection and the maximum strain values are more sensitive than the maximum displacement values to the changes in the Johnson-Cook constitutive model parameters. The results also showed that the influence of changing parameters almost the same on the permanent deflection and maximum strain.

CHAPTER 4

SIMULATION OF THE DYNAMIC RESPONSE OF COLUMN ELEMENTS FOR BLAST LOADING

4.1 Different Axial Loads

As previously stated Nasrr conducted a free-field explosion experiment and gathered data to observe the blast loading characteristics that were presented in the previous chapters. In the material calibration part of this study, the pressure-time history named as 'β loading point 3' was used to represent blast loading. The gathered data from point 3 was used to derive the mentioned pressure-time history by using Modified Friedlander equation. In this part of the study, blast loading history was kept as in the calibrated model, then, in order to analyze the effect of axial load on the beam-column element subjected to blast loading, different axial load and no axial load cases were investigated. It should be noted that in the calibrated model, the W200x71 section was loaded axially with 640 kN which was at 25 % of the column static axial capacity.

Firstly, the no axial load case was examined by comparing the results of the experiment conducted by Nassr (2012) with the results of calibrated model (with no axial load) under same blast load condition. The permanent deflection and the maximum displacement values are given in Table 29. The permanent deflection value of the no axial load case had a 1.83% deviation from the experimental data. Although permanent deflection value of "no axial load" was obtained very close to the experimental result, the maximum displacement value diverged from the experimental one by about 13.01%.

Table 29: Results of test column and calibrated model (no axial load case)

	Permanent Deflection (mm)	Maximum Displacement y-axis (mm)
Test Column no axial load	30.70	62.80
Calibrated model no axial load	30.14	54.63

Table 30: Error percentages for no axial load case

	Error in Permanent Deflection %	Error in Maximum Displacement %
Calibrated model no axial load	1.83%	13.01%

The calibrated model was then examined under different axial loading cases of 40, 50 and 60% of the axial load capacity. The calibrated model was loaded by the load case named as 'β decay 3' based on the blast loading characteristics according to point 3 data. The tabulated results which were obtained by different axial loads on this model can be observed from the following table.

Table 31: Analysis results of different axial load cases for section W200x71 (shot 5)

	Permanent Deflection (mm)	Maximum Displacement y-axis (mm)
no axial load	30.14	54.63
25% of axial load capacity (calibrated model)	30.70	62.80
40% of axial load capacity	50.72	68.73
50% of axial load capacity	60.14	76.55
60% of axial load capacity	82.18	88.88

The permanent deflection and the maximum displacement values increased by 65.20% and 9.45% with respect to the calibrated model as the axial load increased to 40% of the static axial capacity of the column element. Furthermore, as the axial load increased to 50% of the axial capacity, permanent deflection and maximum displacement values increased by 95.91% and 21.89% respectively. Finally the results of the model axially loaded to 60% of the axial capacity showed increase of

the permanent deflection and maximum displacement values by 167.70% and 41.53%, respectively.

Analysis of the displacement time histories for cases with different axial loads showed that the time histories were shifted upward as the axial load increased (Figure 48). In this figure, as the axial load increases, the decrease in the amplitude after the first peak and the slight amount of increase in upward shift can be observed. This behavior is more apparent for the displacement-time history diagram of '60% of the axial load capacity' in Figure 48.

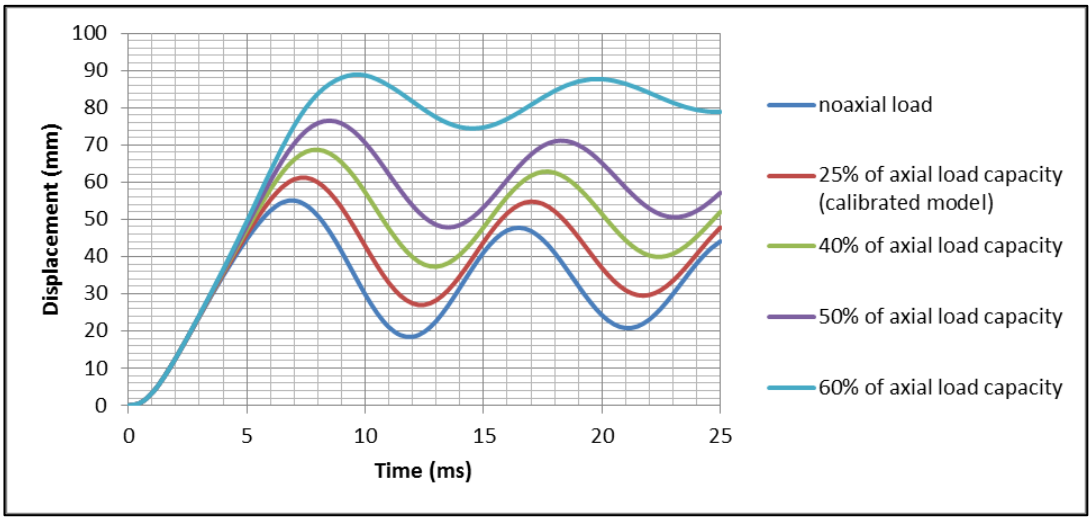

Figure 48: Displacement-Time Histories of different axial load cases

4.2 Different Stand-Off Distances

The blast wave characteristics show varying features depending on the weight of the charge and the stand-off distance. The empirical formulas suggested by different researchers were given in terms of the scaled distance *Z* which is calculated by these two terms. The effect of the different scaled distances on the dynamic response of

beam-column element was examined by changing the stand-off distance while keeping the weight of charge at 250 kg ANFO.

In order to obtain time dependent pressure profile representing the blast loading for different stand-off distances, the software ATBlast (2000) was used. ATBlast is a software developed by the Applied Research Associates, Inc. to calculate the blast load characteristics. According to input of the explosive charge weight, angle of incidence and maximum stand-off distance specified by the user, ATBlast provides the following outputs: Shock Front Velocity (V), Time of Arrival (t_a), Reflected Pressure (P_r), Reflected Impulse (I_r), and positive phase duration (t_d). The results are provided in a tabular format and can be displayed graphically. Graphically displayed curves shows that the blast loading curve is a linear decay function based on the reflected pressure, reflected impulse and positive phase duration.

The effect of stand-off distance was investigated for a deviation of 0.50m from the chosen stand-off value at 9.5m that was used in the chosen experiment set. The stand-off distances studied were 10.50 m and 8.50 m. As the stand-off distance increases, the positive phase duration also increases. On the other hand, it causes a decrease in the reflected pressure and impulse values. The increase in stand-off distance causes inevitable consequences like the decrease in the permanent deflection, maximum displacement, and the maximum strain values. The results of the analyses with varying standoff distances are presented in Table 32. The analysis results showed that the detonation with a clear distance of 9 meters resulted in 60.61 mm permanent deflection while the explosion occurring at 8.50 meters yields a permanent deflection value of 129.77 mm.

Table 32: Results of analysis according to different stand-off distances

	Stand-off Distance	t_d (msec)	Pr (Mpa)	Ir (Mpa.msec)	Permenant Deflection (mm)	Maximum Displacement y-axis (mm)
					32.8	71
Calibrated Model	9.50	10.00	2.1430	3.9375	37.70	61.25
Atblast 10.50	10.50	3.29	1.5018	2.4752	10.59	28.07
Atblast 10.00	10.00	3.01	1.7422	2.6303	19.42	38.13
Atblast 9.50	9.50	2.75	2.0363	2.8049	35.11	54.56
Atblast 9.00	9.00	2.50	2.3993	3.0032	60.61	80.63
Atblast 8.50	8.50	2.26	2.8506	3.2297	129.77	139.72

The reflected pressure and reflected impulse values that are obtained from ATBlast are lower than the recorded values from the experiment as given in Table 32. On the other hand, the deviation from the experimental data is much higher in the parameter positive phase duration. For the point 3, while the recorded positive phase duration is 10 ms, the calculated positive phase duration value is 2.75 ms by ATBlast. The calculated positive phase duration by ATBlast is 47% lower than the smallest recorded t_d at point 5 as 5.2 ms. There was a significant difference between the two reflected impulses. The calculated I_r was 2.8049 MPa.ms which is 29% below the recorded I_r which was 3.9375 MPa.ms. Although the recorded P_r and calculated P_r values are the closest parameters between the experiment and the predictions, the calculated P_r still has a 5 % deviation from the recorded one.

The pressure-time histories that were calculated by the ATBlast software are presented in Figure 49. It is apparent that the loading curves have a linear decay. In order to obtain comparable results, the arrival time for all of the blast loading cases were chosen as 5 ms.

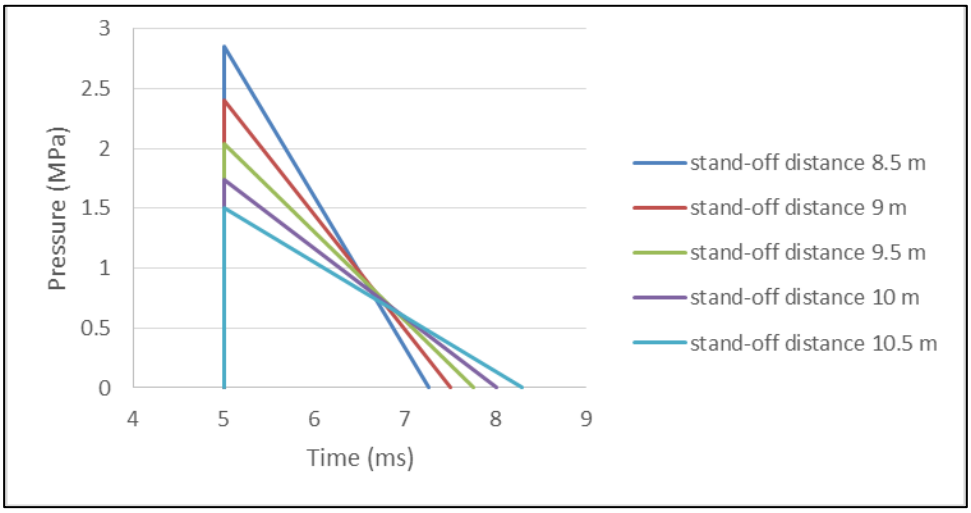

Figure 49: Pressure-Time Histories for different stand-off distances (ATBlast)

The strain-time histories for each loading condition can be seen from Figure 50. It is apparent from the Figure 50 that the strain time histories of the model which has been loaded in accordance with the ATBlast data and the calibrated model (both at a stand-off distance of 9.50m) showed very similar trend.

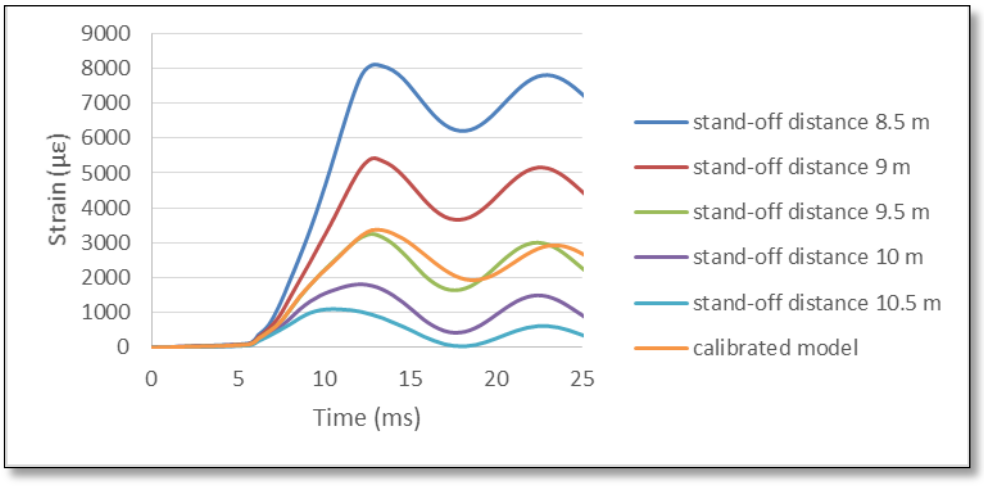

Figure 50: Strain-Time Histories for different stand-off distances

The displacement time histories of the models with different stand-off distances are shown in Figure 51. The model that has been loaded according to ATBlast loading data with a stand-off distance of 9.50 m has a smaller wavelength than the calibrated model. This situation is likely caused by short loading duration of ATBlast prediction which is 2.75 ms with respect to calibrated model which has a loading duration equal to 8.9 ms.

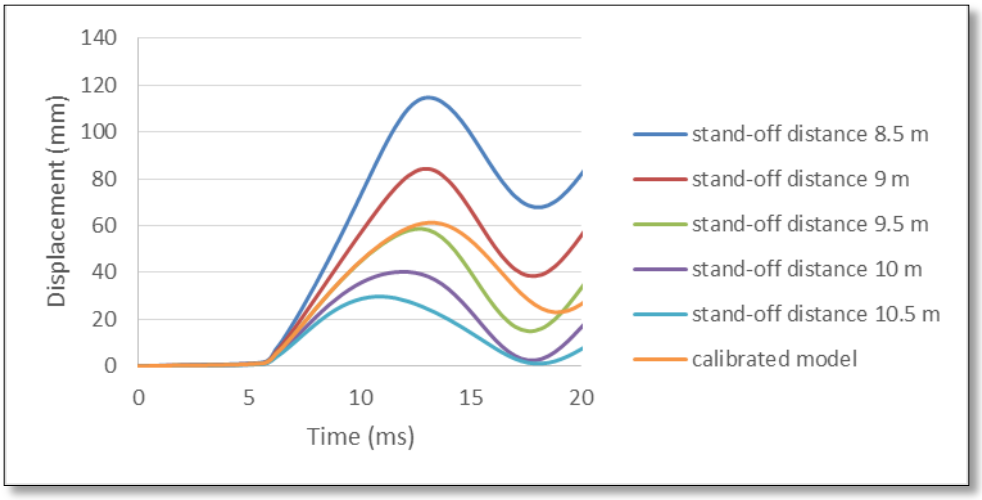

Figure 51: Pressure-Time Histories for different stand-off distances

4.3 Different Axial Load Conditions and Stand-off Distances

In this section, the effects of different axial load cases were examined for different stand-off distances. In the calibrated model of 'shot 5', the section W200x71, was loaded at 25% of its static axial capacity. In order to examine the influence of axial load on the maximum displacement, no axial load case and columns loaded at 40, 50 and 60% of the axial load capacity were analyzed for different stand-off distances. The blast load characteristics, i.e. the reflected pressure P_r, reflected impulse I_r and positive phase duration t_d values were obtained by using the ATBlast software for

different stand-off distances in a range of 8 m and 10.5 m for a charge weight of 250 kg ANFO.

In the following figure, the resulting maximum displacement values of each model loaded at different axial loads are given in mm. As shown in Figure 52, both the applied axial load and the stand-off distance play a very important role for the beam-column elements. The maximum displacement values for the no axial load case with blast loading according to different stand-off distances shows a reasonable trend, with the displacement of the column increasing somewhat quadratically with decreasing stand-off distance. On the other hand, it can be said that as the axial load increases, the given section fails (crushes) if the charge is set closer than a minimum stand-off distance. For a W200x71 section initially loaded at 50% axial load capacity, a blast wave caused by a 250kg ANFO at lower than 9.125 m clear distance leads to the failure of the column. When the section was initially axially loaded at 60% of its axial load capacity, the analysis showed that a clear distance less than 9.5m causes a failure of the column by losing its structural integrity.

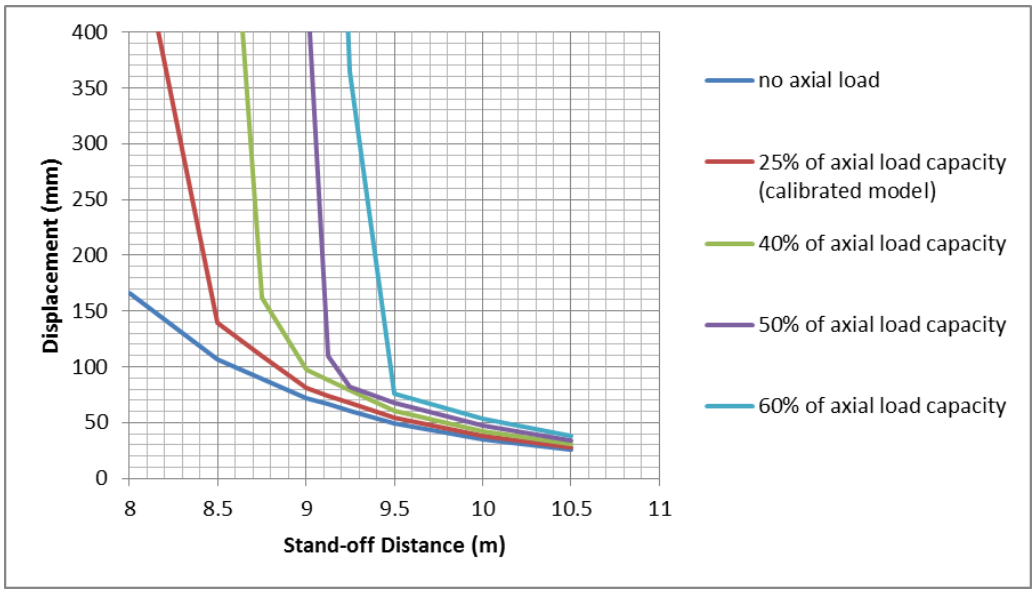

Figure 52: Maximum displacement values at different stand-off distances for each axial load cases

4.4 Different Boundary Conditions

In order to examine effect of boundary condition on the dynamic response of steel beam to blast loading, the model was simulated with a fixed boundary condition at ends. The strain–time histories of this fixed beam model and the simply supported beams are compared. The effect of the boundary condition was compared for the system with no initial axial load.

The strain time histories for the models with different boundary conditions are presented in Figure 53. Maximum strain value of the system with fixed conditions is 726 με which is 63% lower than the maximum strain value of simply supported beam at 1980 με.

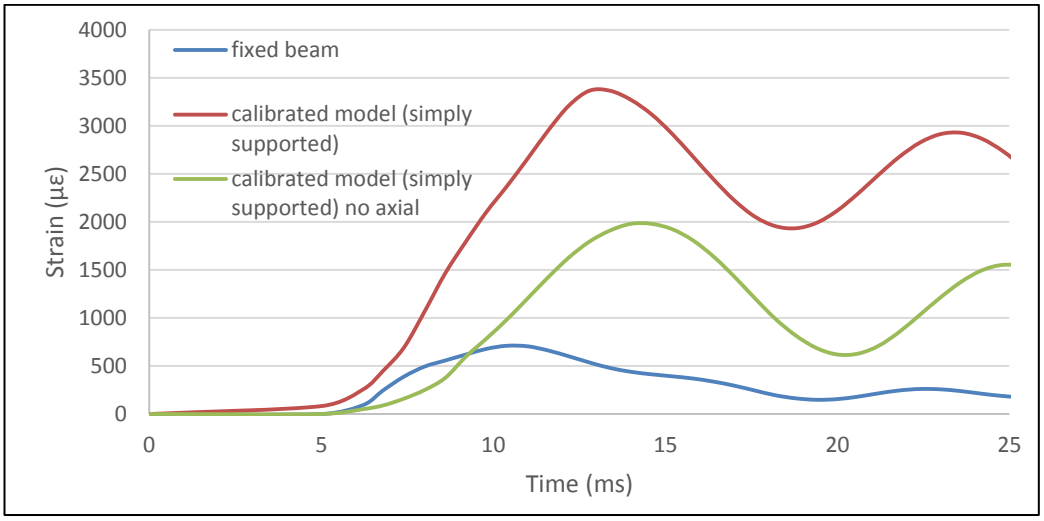

Figure 53: Strain-Time Histories for Different Boundary Conditions

The displacement time histories for the model with different boundary conditions are presented in Figure 54. The maximum displacement value is 21.06 mm and 47.80 mm for the fixed beam and the simply supported beam, respectively. The maximum

displacement value of the fixed end beam is 56% lower than the maximum displacement value of the simply supported beam.

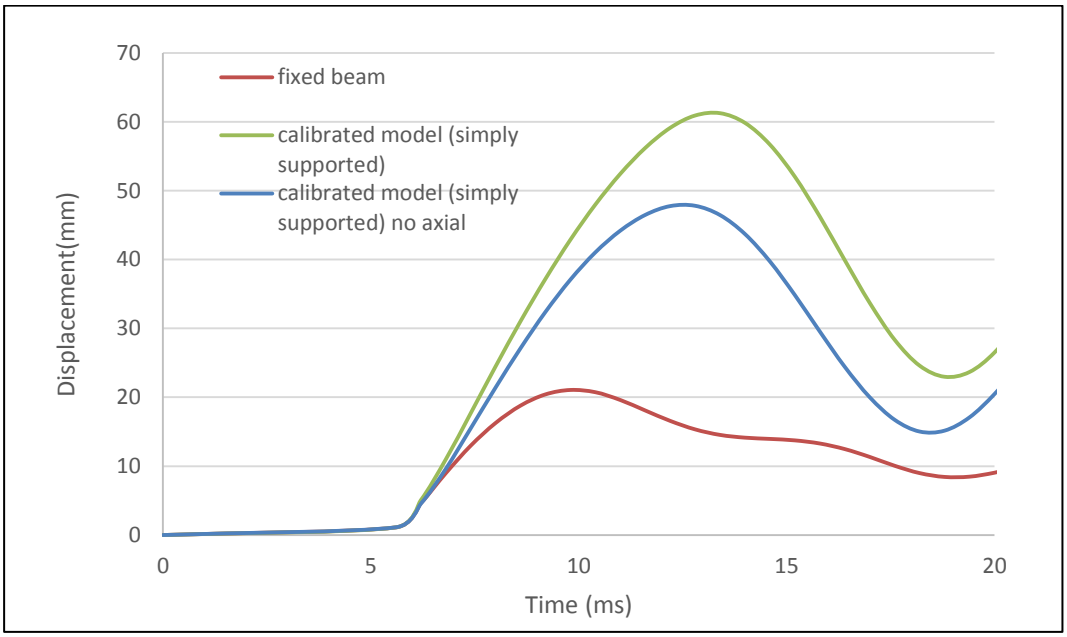

Figure 54: Displacement-Time Histories for Different Bounday Conditions

CHAPTER 5

CONCLUSION

In this study, the three dimensional dynamic response of steel beam-column elements subjected to the blast loading was investigated with the goal of determining the effect of the chosen material, loading and modeling conditions on the prediction results. Parametric studies affecting the dynamic behavior of the beam-column elements were conducted using different empirical models suggested in the literature and relevant assumptions. Conclusions from these analyses can be summarized as follows:

- Empirical formulas suggested by many researchers to estimate the blast wave characteristics resulted in lower values than the experimental results.
- The simulation model was calibrated to two different experiments. The results of the calibration showed that the modeling assumptions and the material properties used in the calibration represent the testing conditions well. The results from the calibrated models and the experiment agreed well.
- The parametric study conducted to observe influence of J-C constitutive model parameters showed that the most effective parameter influencing the the displacement and strain values of the simulation model is the parameter ‘A’ followed by parameter ‘n’.
- As the parameters ‘A’, ‘B’ and ‘C’ increased, it was observed that the displacement experienced by the column was decreased. As expected, a reduction in these parameters led to an increase in the displacement and strain values.
- The results showed that the change in parameter values caused different rate of change on the displacement and strain values. The permanent deflection

and the maximum strain values are the more sensitive than the maximum displacement values to the changes in Johnson-Cook constitutive model parameters.

- The reduction in the values of the parameters yielded more change on the simulation results compared to the increase in the values.
- The results also showed that the influence of changing parameters was almost the same on the permanent deflection and the maximum strain.
- ATBlast software outputs were used to obtain blast load parameters to observe the dynamic response of steel beam-column to blast loading that have different stand-off distances. The blast wave characteristics such as positive phase duration, reflected impulse and reflected pressure that are calculated by ATBlast are again lower than the experimental data. For instance, the calculated I_r was 2.8049 MPa.ms which is the 29% below than the recorded I_r which was 3.9375 MPa.ms.
- As the stand-off distance decreased, it was observed that the element becomes more vulnerable to the blast effect. In addition to that, as the detonation occurs at 8.50 meters there occurs twice as much permanent deflection as in the case of 9.0 meters stand-off distance.
- The examination of the effect of the axial load on the column at varying stand-off distances showed a clear failure distance that should be preserved for columns with higher axial loads. The W200x71 steel section loaded by 25% of its axial capacity loses its structural integrity when subjected to a blast load caused by the detonation of 250 kg ANFO at a distance closer than 8.5 meters. For the same charge, the section loaded at 60% of its axial capacity is crushed for a stand-off distance lower than 9.50 meters.
- The maximum strain and maximum displacement of the finite element models were compared for fixed end and simply supported boundary conditions, representing different construction choices for a column. Maximum strain value of fixed beam is 726 με which is 63 % lower than the maximum strain value of simply supported beam at 1980 με. Although the simply supported beam undergoes plastic deformation, fixed beam remains at elastic range under the same blast loading condition. The maximum

displacement values for the fixed and the simply supported beam is 21.06 mm and 47.80 mm, respectively. Maximum displacement of the fixed beam was 56% lower than the corresponding value of the simply supported beam.

The finite element model that established in this research to investigate the dynamic response of W200X71 steel section could be used in finite element analysis of frame systems. The progressive collapse situations could be investigated by introducing damage model to finite element model material properties.

REFERENCES

Armstrong, R. W., & Walley, S. M. (2008). High strain rate properties of metals and alloys. *International Materials Reviews, 53*(3), 105–128.

ABAQUS, (2010). Analysis user's manual 6.10-EF, Dassault Systems Simulia Corp., Providence, RI, USA

Assal T. Hussein (2010). Non-Linear Analysis of SDOF Systems under Blast Load. *European Journal of Scientific Research, 45(*3), 430–437.

ATBlast, (2007). A computer software by Protective Glazing Council. *Applied Research Associates (ARA), Inc., USA.*

Baker, W. E. (1973). Explosions in Air. *University of Texas Press, Austin, Texas.*

Baker, W. E., Cox, P. A., Westine, P. S., Kulesz, J. J., Strehlow, R. A. (1983). *Explosion Hazards and Evaluation.*Elsevier Scientific Publishing Co.

Bogosian D., Ferrito J., & Shi, Y. (2002). *Measuring uncertainty and conservatism in simplified blast models.* Proc 30th Explosion Safety Seminar, Atlanta, GA.

Brode, H. L. (1955). Numerical solutions of spherical blast waves. *Journal of Applied Physics, 26,* 766.

Brode, H. (1958). A Calculation of the Blast Wave from a Spherical Charge of TNT. *ASTIA Document Number AD 144302*. Retrieved from

Cabello, B. (2011). Dynamic Stress Analysis of the effect of an Air Blast Wave on a Stainless Steel Plate.

Carlucci, P., Mougeotte, C., Recchia, S., & Ji, H. (2010). Novel Approach to Conducting Blast Load Analyses Using Abaqus/Explicit-CEL, 1–15. Retrieved from http://www.stormingmedia.us/57/5718/A571855.html

Defence Research & Development Canada http://www.drdc-rddc.gc.ca/en/dynamic-article.page?doc=drdc-s-experimental-proving-ground-supports-caf-allied-readiness/i6mizy83 "last accessed date 21.03.16"

Dewey, J. M. (1964). The air velocity in blast waves from TNT explosions. *Proc. of the Royal Society, A, No.279, (366-385).*

Gambirasio, L., & Rizzi, E. (2014). On the calibration strategies of the Johnson–Cook strength model: Discussion and applications to experimental data. *Material Science and Engineering A 610:370-413.*

Glasstone, S., & Dolan, P. J. (1977). The Effects of Nuclear Weapons. *United States Department of Defense & The Energy Research and Development Administration, Washington, D.C. 20402.*

Eichinger, W. E. (1985). Mach Stem Modelling with Spherical Shock Waves. *Defence Technical Information Center AD-A159 214.*

Gao, Y., Xu, C., He, Z., He, Y., & Li, L. (2015). Response Characteristics and Adiabatic Heating during High Strain Rate for TRIP Steel and DP Steel. *Journal of Iron and Steel Research, International, 22(1),*48-54.

Guzas, E. L., & Earls, C. J. (2011). Simulating blast effects on steel beam-column members: Applications. *Computers & Structures*, *89*(23-24), 2149–2161.

Heidarpour, A., & Bradford, M. A. (2011). Beam–column element for non-linear dynamic analysis of steel members subjected to blast loading. *Engineering Structures*, *33*(4), 1259–1266.

Henrych, J. (1979). The dynamics of explosion and its use. *Elsevier Scientific Publishing Company, New York, USA.*

Hugoniot, P.H. (1st part, 1887), 58: 1-125 (2nd part, 1889). Mémoire sur la propagation du mouvement dans les corps et plus spécialement dans les gas parfaits, J. de l´École Poly-technique, 57: 3-97.

Hyde, D.W. (1990). Conventional weapons effect (CONWEP). *Application of TM5-855-1. US Army Engineer Waterways Experiment Station, Vicksburg,USA.*

Hopkinson, B. (1915). British Ordnance Board Minutes 13565

Itabashi, M., & Kawata, K. (2000). Carbon content effect on high-strain-rate tensile

properties for carbon steels. *International Journal of Impact Engineering*, 24 (2), 117-131.

Jones, N. (1988). Structural Impact. *Cambridge University Press, Cambridge;New York.*

Johnson, G. R., & Cook, W. H. (1983). A constitutive model and data for metals subjected to large strains, high strain rates and high temperatures. *7th International Symposium on Ballistics*.

Jutras, M. (2008). Improvement of the characterisation method of the Johnson-Cook model, 65.

Kingery, C.N., & Bulmash, G. (1984). *Airblast Parameters from TNT Spherical Air Burst and Hemispherical Surface Burst*. Report ARBL-TR-02555. US Army Research and Development Centre – Ballistic Research Laboratory (BRL), Aberdeen Proving Ground, Aberdeen, MD.

Kinney, G.F., Graham, K.J., 1985. *Explosive shocks in air*. Springer-Verlag, New York.

Larcher, M. (Joint R. C. (2008). Pressure-Time Functions for the Description of Air Blast Waves, 1–32.

Lee, K., Kim, T., & Kim, J. (2009). Local response of W-shaped steel columns under blast loading. *Structural Engineering and Mechanics*, *31*(1), 25–38.

Liew, J. Y. R. (2008). Survivability of steel frame structures subject to blast and fire. *Journal of Constructional Steel Research*, *64*(7-8), 854–866.

LS-DYNA Keyword User's Manual, Version 971, (2013). Livermore Software Technology Corporation, Livermore, California: Livermore Software Technology Corporation

Magallanes, J. M., & Koenig, J. W. (2006). Experimental Results of the Aisc Full - Scale Column BLast Test Aisc Full -Scale Column Blast.

Majzoobi, G. H., Mahmoudi A. H. & Moradi S. (2016) Ductile to Brittle Failure Transition of HSLA-100 Steel at High Strain Rates and Subzero Temperatures. *Engineering Fracture Mechanics, 158,* 179-193.

Mays, G. C., & Smith, P. D. (1995). Blast effects on buildings.

Mckay, A., Bazan, M., Marchand, K., Gomez, M., & Benshoof, P. (n.d.) (2011). Steel Frame Structure Performance in Blast Environments. *14th International Symposium on Interaction of the Effects of Munitions with Structures*

Mougeotte, C., Carlucci, P., Recchia, S. & Ji, H. (2010). *Novel Approach to Conducting Blast Load Analyses Using Abaqus/Explicit-CEL*.2010 SIMULIA Customer Conference

Needham, C. E. (2010). Formation of Blast Waves. *Blast Waves, Shock Wave and High Pressure Phenomena*, 17-36.

Ngo, T., Mendis, P., Gupta, a, & Ramsay, J. (2007). Blast loading and blast effects on structures–an overview. *Electronic Journal of Structural …*, (Loading on Structures), 76–91.

Özel, T., & Karpat, Y. (2007). Identification of Constitutive Material Model Parameters for High-Strain Rate Metal Cutting Conditions Using Evolutionary Computational Algorithms. *Materials and Manufacturing Processes*, *22*(5), 659–667.

Polcyn, M. A., & Myers, K. D. (n.d.). Use of SBEDS for Blast Resistant Design in accordance with UFC 3-340-02, *02*(210), 12.

Ramesh, K.(2008). High rates and impact experiments. Springer handbook of experimental solid mechanics. *Springer US*. 929–960.

Rankine, W. J. M. (1870). On the thermodynamic theory of waves of finite longitudinal disturbance. *Phil. Trans. (of the R. Soc. of London), 160/II, 1870, 277-288.*

Sach, R. G. (1944). *The Dependence of Blast on Ambient Pressure and Temperature*. BRL Report No. 466, Aberdeen Proving Ground

Smith, P. D., & Hetherington, J. G. (1994). Blast and ballistic loading of structures. *Butterworth-Heinemann, Oxford; Boston.*

United Nations Office for Disarmament Affairs. (2013). International ammunition technical guidelines, IATG 01.80:2011[E].

USDOD, (2008). Structures to resist the effects of accidential explosions. *Document No. UFC 3-340-02.* US Department of Defence (USDOD), Washington, DC.

Yang, Z. (1997). Finite element simulation of response of buried shelters to blast loadings. *Finite Elements in Analysis and Design*, *24*(3), 113–132.

APPENDIX A

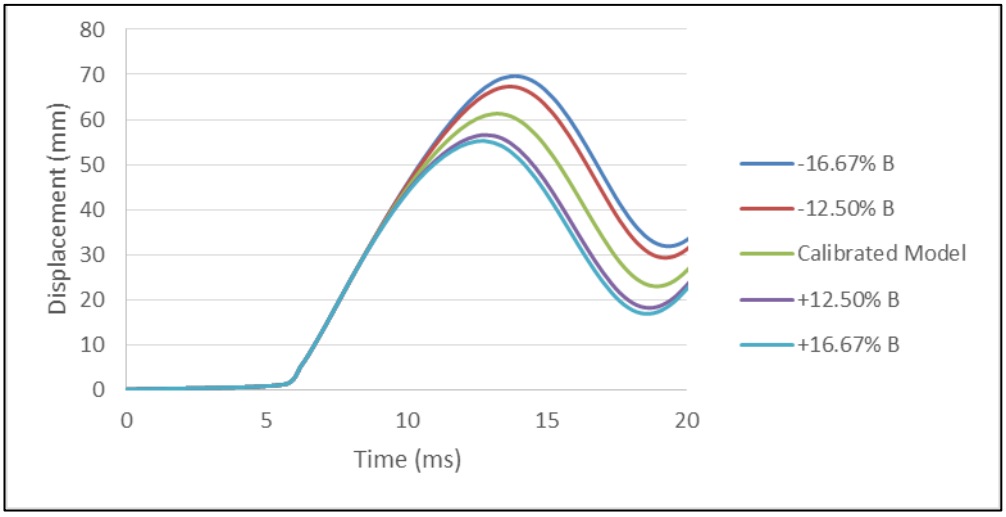

Figure 55: A.1 Parameter 'B' - Displacement time history

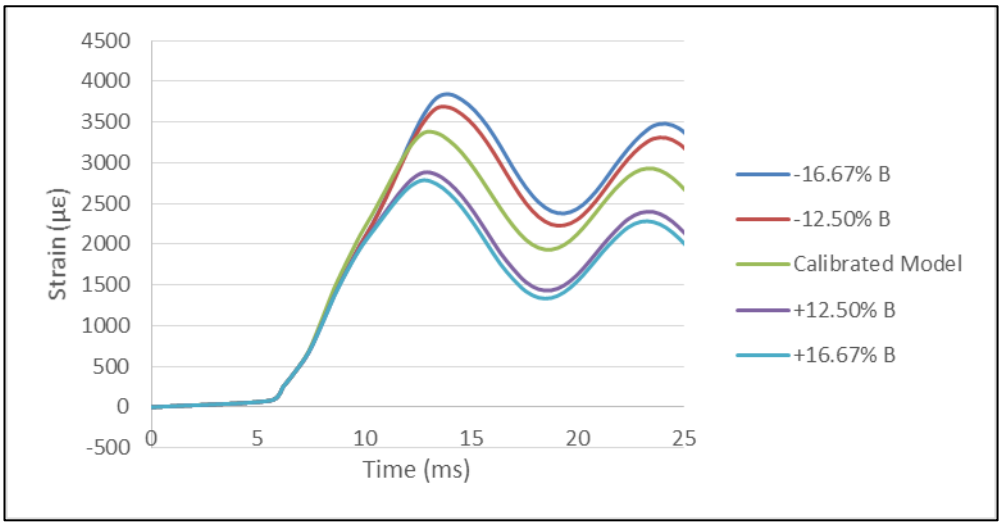

Figure 56: A.2 Parameter 'B' - Strain time history

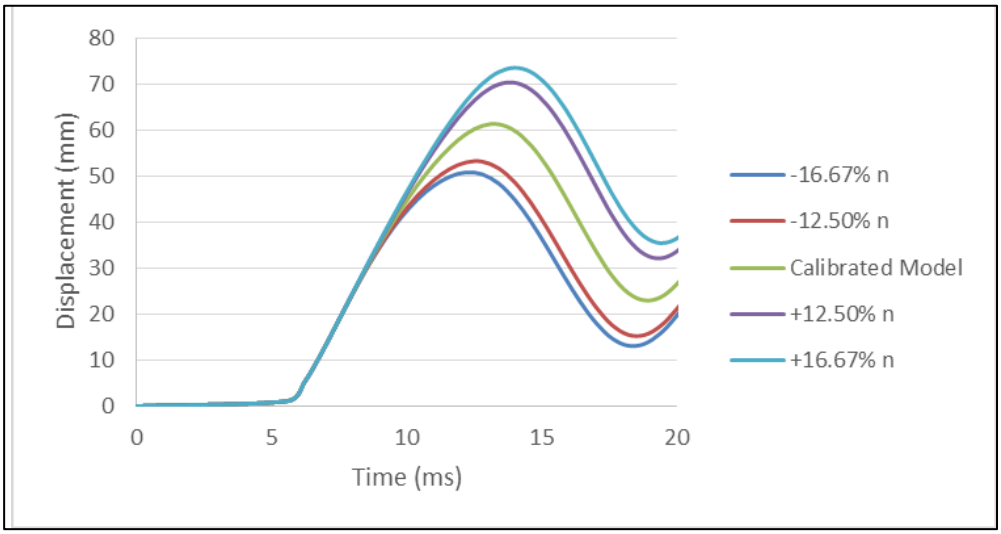

Figure 57: A.3 Parameter 'n' - Displacement time history

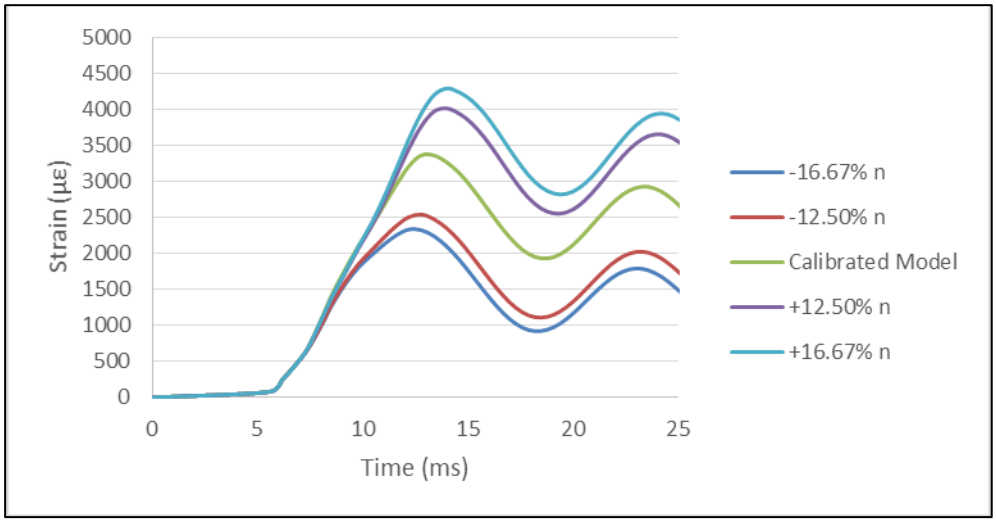

Figure 58: A.4 Parameter 'n' - Strain time history

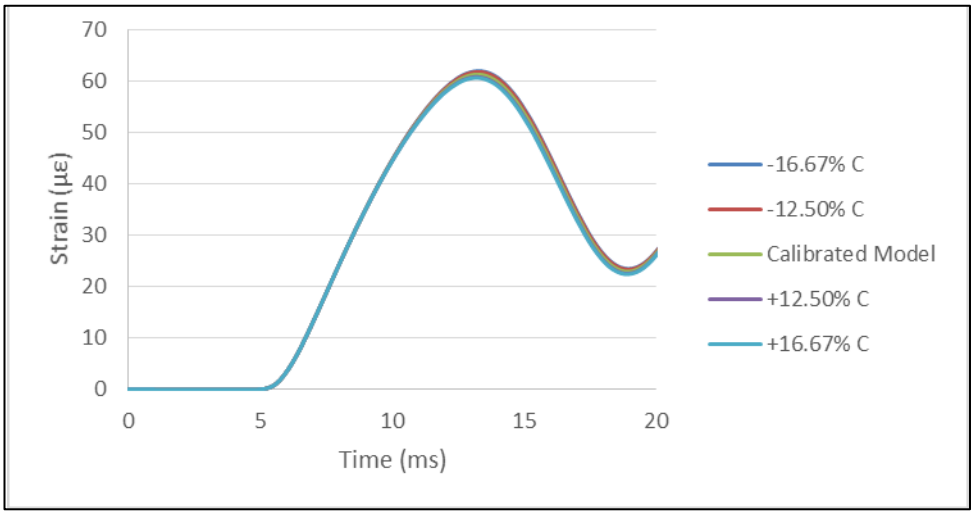

Figure 59 A.5 Parameter 'C' - Displacement time history

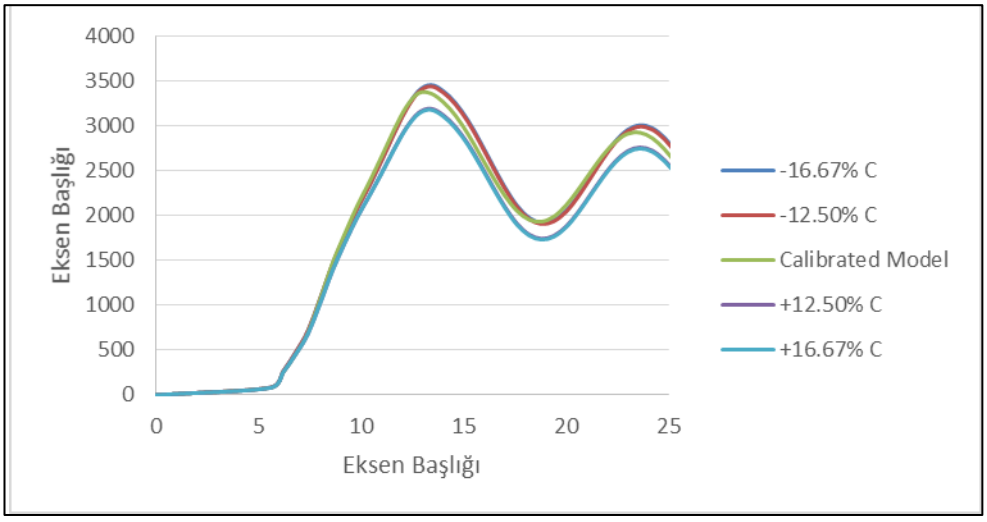

Figure 60 A.6 Parameter 'C' - Strain time history

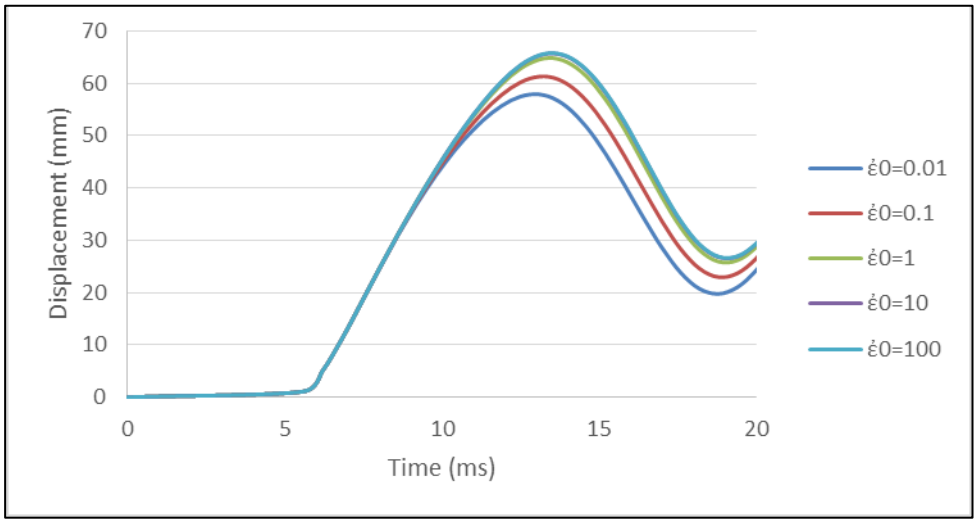

Figure 61 A.7 Parameter ' $\dot{\varepsilon}_0$ ' -- Displacement time history

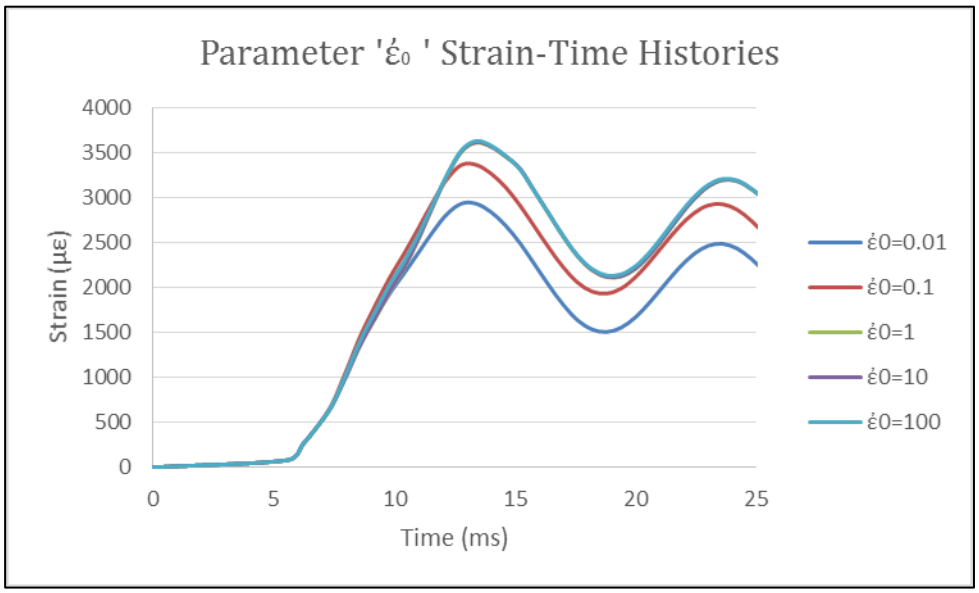

Figure 62 A.8 Parameter ' $\dot{\varepsilon}_0$ ' - Strain time history

APPENDIX B

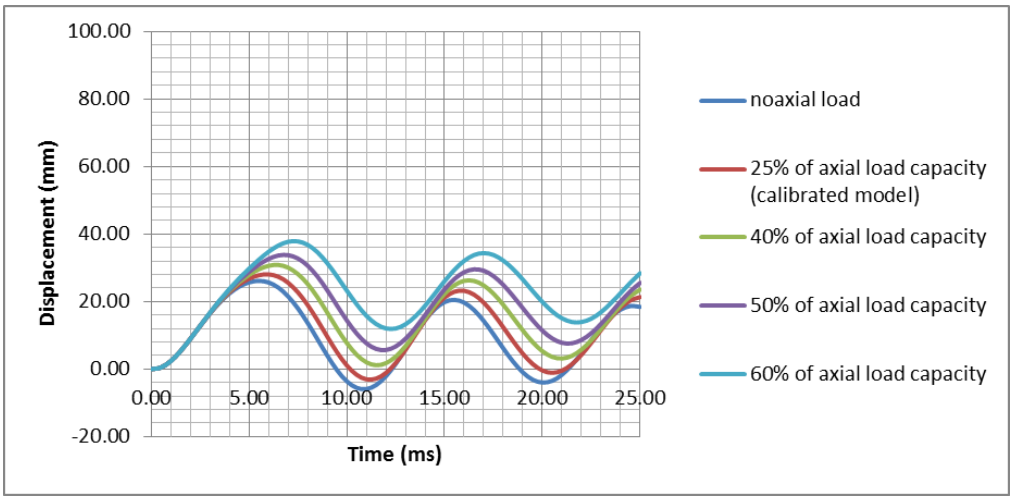

Figure 63 B.1 Displacement-time histories for different axial load cases at stand-off distance 10.5m

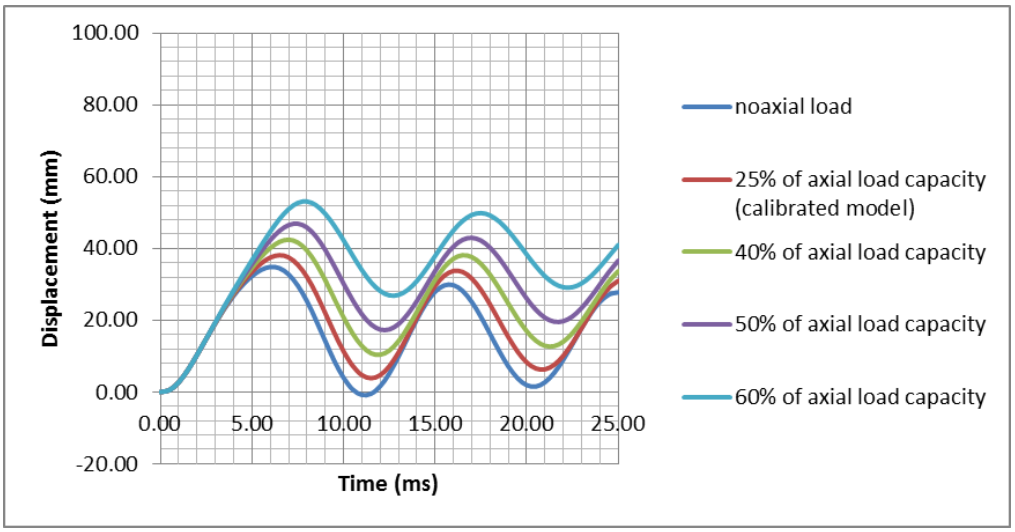

Figure 64 B.2 Displacement-time histories for different axial load cases at stand-off distance 10.0m

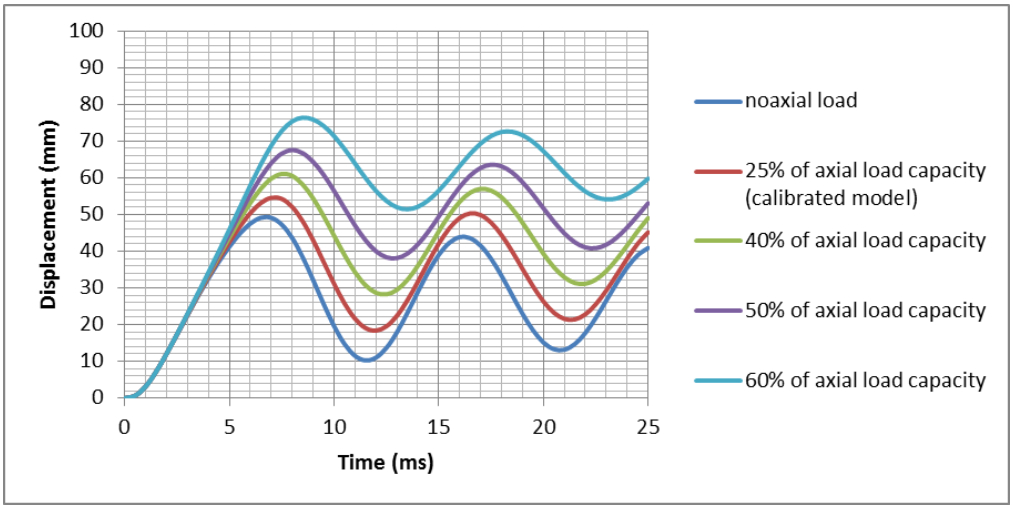

Figure 65 B.3 Displacement-time histories for different axial load cases at stand-off distance 9.5 m

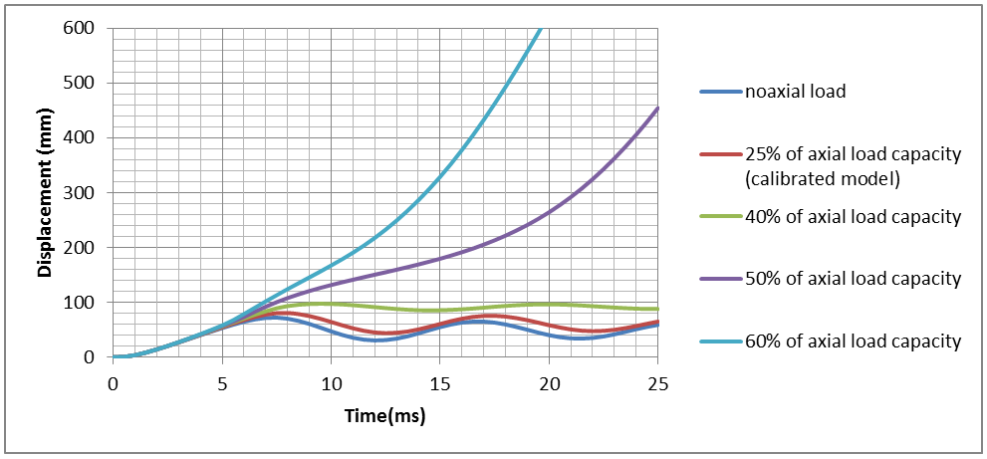

Figure 66 B.4 Displacement-time histories for different axial load cases at stand-off distance 9.0 m

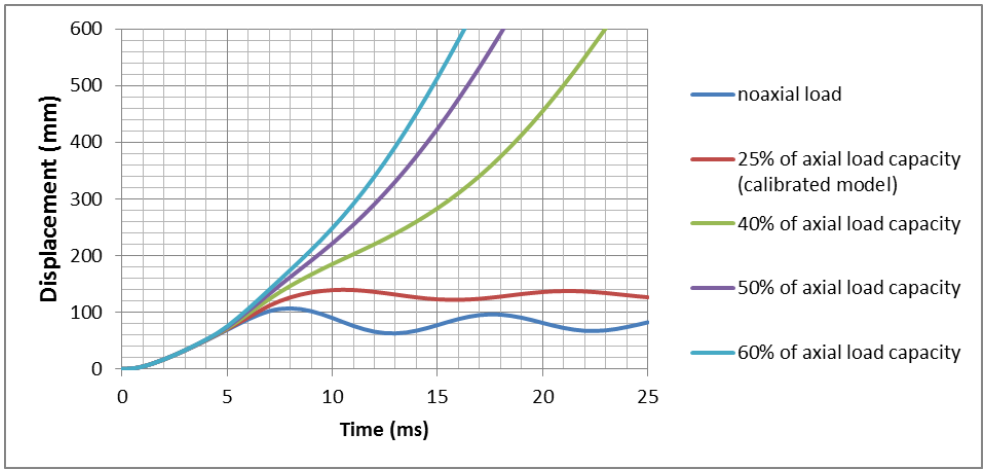

Figure 67 B.5 Displacement-time histories for different axial load cases at stand-off distance 8.5 m